Role of cerebrovascular abnormalities in the 16p11.2 deletion autism syndrome

Julie Ouellette

Thesis submitted to the
Faculty of Graduate and Postdoctoral Studies
in partial fulfillment of the requirements
for the Master of Science degree in Neuroscience

Department of Cellular and Molecular Medicine

Faculty of Medicine

University of Ottawa

Abstract

Brain development and function rely on vascular features that ensure adequate supply of oxygen and nutrients from the blood stream. These features consist of a well-established vascular network, a functional blood-brain barrier, as well as cerebral blood flow regulation. Early life impairments in these features can lead to neurodevelopmental defects. Very few studies have considered the contribution of the brain vasculature to autism spectrum disorders (ASD). A recent postmortem study in young ASD brains suggested an impairment in angiogenesis, a process through which new vessels are formed. A possible link between ASD and altered cerebral perfusion has also been suggested by functional imaging studies. Yet, contribution of cerebrovascular deficits to ASD physiopathology remains elusive, hence a detailed analysis of these deficits is needed.

ASD are viewed as neurodevelopmental conditions associated with genetic origins. Mutations identified as a possible cause for ASD include the common 16p11.2 deletion, which leads to the haploinsufficiency of approximately 30 highly-conserved genes. In this thesis, we are using a multidisciplinary approach in order to decipher the cerebrovascular underpinnings of ASD in a mouse model of the 16p11.2 deletion syndrome (*16p11.2*$^{df/+}$ mice). We have identified functional and structural cerebrovascular deficits during postnatal development in constitutive *16p11.2*$^{df/+}$ mutants. In particular, *16p11.2* $^{df/+}$ mice display a significant decrease in microvascular branching and density in the cerebral cortex at P14 when compared to age-matched WT littermates. In addition, *16p11.2*$^{df/+}$ mice display a collection of functional abnormalities at P50 when compared to WT mice, such as altered neurovascular coupling *in vivo* and altered vascular reactivity *ex vivo*. Notably, we demonstrated a defective endothelium-dependent vasodilation in *16p11.2*$^{df/+}$ mice, while smooth muscle function is unaffected. Furthermore, we generated mice harboring the endothelial-specific 16p11.2 haploinsufficiency (*Cdh5-Cre*$^{tg/+}$;*16p11.2*$^{flox/+}$) in order to dissect the endothelial

contribution to ASD phenotypes. These mice underwent behavioral testing to assess whether they display 16p11.2 syndrome -related characteristics. We demonstrated that these conditional mutant mice show home cage hyperactivity in the beam break test, repetitive behaviors in the marble burying test, as well as motor coordination deficits in the rotarod test.

Our findings thus establish endothelial cells as key contributors to the pathophysiology of the 16p11.2 deletion syndrome, and provide novel insight into how the cerebral endothelium fine-tunes brain maturation.

Table of Contents

List of Figures

List of Abbreviations

Aβ	Amyloid beta
AD	Alzheimer's Disease
ALS	Amyotrophic Lateral Sclerosis
AMPA	α-amino-3-hydroxy-5-methyl-4-isoxazolepropionic acid
ANOVA	Analysis of variance
ASD	Autism Spectrum Disorders
ASL-MRI	Arterial spin labeling- magnetic resonance imaging
BBB	Blood-brain barrier
BCKDK	Branched chain keto-acid dehydrogenase kinase
BOLD	Blood-oxygen-level dependent imaging
CADASIL	Cerebral autosomal dominant arteriopathy with sub-cortical infarcts and leukoencephalopathy
CBF	Cerebral blood flow
cECs	Cortical endothelial cells
CNS	Central nervous system
CNV	Copy number variations
DEG	Differentially expressed genes
DSM-5	Diagnostic and statistical manual of mental disorders 5th edition
ECs	Endothelial cells
EEG	Electroencephalogram
eNOS	Endothelial nitric oxide synthase
FC	Functional connectivity

fcMRI	Functional connectivity magnetic resonance imaging
FDG-PET	Fluorodeoxyglucose- positron emission tomography
fMRI	Functional magnetic resonance imaging
GABA	gamma-Aminobutyric acid
GLUT1	Glucose transporter 1
HD	Huntington's disease
HIF-1	Hypoxia-inducible factors
ICC	Immunocytochemistry
IHC	Immunohistochemistry
LAT1	Large neutral amino acid transporter
LDF	Laser Doppler flowmetry
MCA	Middle cerebral artery
MNFA	Matrigel-based network formation assay
NASS	National autism spectrum disorder surveillance system
NO	Nitric oxide
NPC	Neural progenitor cells
NVC	Neurovascular coupling
NVU	Neurovascular unit
PD	Parkinson's disease
PET	Positron emission tomography
qPCR	Quantitative polymerase chain reaction
rCBF	Regional cerebral blood flow
SMC	Smooth muscle cells

sO_2	Oxygen saturation
SPECT	Single-photon emission computed tomography
TEM	Transmission electron microscopy
USVs	Ultrasonic vocalizations
VE-Cadherin	Vascular endothelial- cadherin
VEGF	Vascular endothelial growth factor
VR	Vascular reactivity
VSMC	Vascular smooth muscle cells
WT	Wild type

Acknowledgments

First and foremost, I would like to express my sincere gratitude to Dr. Baptiste Lacoste for the opportunity to complete my M.Sc. in Neuroscience in his laboratory. His extensive knowledge and experience as well as his continuous support and enthusiasm for my M.Sc. study has allowed me to gain experience in, and be exposed to a new upcoming field.

I would like to extend my gratitude to all former and present members of Dr. Lacoste's laboratory, as well as numerous precious collaborators. Their advice and technical assistance, and collaborative efforts made this ambitious project possible. Contributions of all are invaluable for this thesis (as detailed on the following page).

Additionally, I would like to thank all of our collaborators for their help and contribution on this project. All aspect studied were of great importance for its completion. These collaborations have allowed me to expand my knowledge and expertise on new techniques in order to study different avenues of the cerebral vasculature. A special thanks to Dr. Mirabelle Ho, for her help and continuous involvement in this project.

My sincere thanks to the Behavior Core, Drs. Kerstin Ure and Diane Lagace, and Mirela Barclay, for the time they took out of their busy schedules to train and provide me with assistance when required. Thank you Dr. Jean-Claude Béïque, Dr. Simon Chen and Dr. Dylan Burger for agreeing to act as my Master's degree Thesis Advisory Committee members and for providing me feedback on this study.

Last but not least, I would like to sincerely thank my family and friends for the inspiration, support and motivation throughout this process.

Statement of contributions:

Julie Ouellette completed all behavioral testing and analysis (see Figure 3, page 38)

Julie Ouellette and Dr. Xavier Toussay completed contrast imaging and photoacoustic imaging (PAI) from FUJIFILM VisualSonics, Inc. facility (Toronto, ON), with help of their science specialist Melissa Yin (see Figure 4, page 41 and Figure 7C-D, page 44).

Julie Ouellette completed analysis of all contrast imaging and PAI data (see Figure 4, page 41 and Figure 7C-D, page 44)

Dr. Xavier Toussay completed and analyzed LDF data (see Figure 5A, page 42, Figure 6 page 43 and Figure 15 page 56).

Julie Ouellette completed and analyzed blood pressure data (see Figure 5B, page 42 and Figure 15, page 56)

Alexia Kirby and Dr. Adam J. Shuhendler (Faculty of Science, Department of Chemistry and Biomolecular Sciences, University of Ottawa) completed and analyzed FDG-PET scan results (see Figure 7A-B, page 44)

Dr. María Lacalle-Aurioles (Laboratory of Cerebrovascular Research, Montreal Neurological Institute, McGill University) completed and analyzed vascular reactivity of middle cerebral artery (see Figure 8A-C, page 46)

Drs. Jean-François Thibodeau and Christopher R. Kennedy (Kidney Research Center, Ottawa Hospital Research Institute) completed and analyzed vascular reactivity of mesenteric artery (see Figure 8D, page 46)

Julie Ouellette completed immunohistochemistry and imaging of all vascular network and NVU studies (see Figure 9, page 47; Figure 10, page 48; Figure 11, page 49)

Julie Ouellette analyzed NVU cell density and coverage (see Figure 11, page 49)

Drs. Cesar H. Comin (Department of Computer Science, Federal University of São Carlos) and Luciano da F. Costa (São Carlos Institute of Physics, FCM-USP, University of São Paulo) completed computational morphometric analysis of 3D vascular image stacks (see Figure 9, page 47 and Figure 10, page 48)

Micaël Carrier and Dr. Marie-Ève Tremblay (Axe neurosciences, Centre de recherche du CHU de Québec-Université Laval) performed TEM on our samples (see Figure 11A and C, page 49).

Peter Van Dykan (Lacoste lab) analyzed TEM images for astrocytic endfeet quantifications.

Julie Ouellette completed all primary brain endothelial cell isolations for immunocytochemistry, Matrigel-based assays, RNA extraction, RT-qPCR.

Julie Ouellette and Dr. Mirabelle Ho (Stewart lab, Regenerative Medicine Program, Ottawa Hospital Research Institute) completed matrigel assays using murine endothelial cells (see Figure 13A, page 52).

Julie Ouellette performed and analyzed cell cycle analysis on murine endothelial cells (see Figure 13B, page 52).

Julie Ouellette and Dr. Moises Freitas-Andrade completed structural analysis of *16p11.2*^{vasc} mice (see Figure 14, page 55).

1. Introduction

1.1. Brain vasculature importance in development

The brain accounts for very little of a person's body mass (~2%); however, it requires 25% of the cardiac output for proper blood perfusion to match metabolic needs [1-4]. Normal brain function hence relies on a healthy vasculature to match blood supply to metabolic demands of neural cells [3, 5, 6]. The human brain contains approximately 100 billion vessels (~600km), all of which are critical for the delivery of nutrients and oxygen to brain cells [7]. As such, to ensure appropriate brain maturation and function, the brain is dependent on key vascular features: 1) a dense vasculature; 2) a tightly-controlled environment ensured by the blood-brain barrier (BBB); and 3) the regulation of cerebral blood flow (CBF) via neurovascular coupling (NVC) mechanisms [2, 5]. This NVC consists of neural and vascular cells forming a functionally integrated network, where increased neural activity leads to increased CBF [8, 9]. This response is made possible by the close anatomical apposition between nervous and vascular systems [9]. The anatomical substrate of NVC consists of a multicellular system called the neurovascular unit (NVU), in which pericytes, astrocytes, neurons, and endothelial cells work together to control vessel diameter (i.e. CBF) to ensure proper supply of oxygen and nutrients to the brain [10]. In addition, NVU cells are required for the integrity of the BBB, which maintains brain homeostasis [5, 6, 10].

During early embryonic development, the brain vasculature has a surmounting role in providing oxygen to developing neural cells in otherwise hypoxic tissues. These immature cells require a lot of energy to maintain a proper course of development [11]. Increased energy consumption by neural cells creates a hypoxic environment. The brain utilizes this state as a signal for an increase production of blood vessels for the adequate delivery of oxygen and nutrients [5, 12]. These signals include hypoxia-induced vascular endothelial growth factor (VEGF) to initiate

vessel ingression into deep brain structures and vascular patterning [5]. In addition to a hypoxic environment as a stimulant for vascular development, the embryonic central nervous system (CNS) requires neural cells to stimulate vessel growth by releasing pro-angiogenic factors [13]. Consequently, the neural environment plays a role in the initial ingression (embryonic day 10, E10), elaboration, and pruning of blood vessels. Similarly, vessels (i.e. endothelial cells) instruct neural cells to divide and differentiate by releasing paracrine signals that promote neuronal development [5, 13-15]. Although, the precise mechanisms involved have not been determined, it has been suggested that neural progenitor cells (NPCs) secrete VEGF, proangiogenic factor, to promote CNS vascularization[16]. Moreover, endothelial cells release BDNF and neurotrophins to regulate neurogenesis [13]. This neuro-vascular crosstalk demonstrates that, in the developing brain, neuronal and vascular system coordinate their establishment [17]. Throughout development the vascular network remodels until the system can ensure a stable network and optimal blood flow to actively respond to the increasing neural activity. Studies have shown that a lack of this vascular-neural crosstalk can display cortical defects indirectly through compromised vasculature [18-20]. Thus, shared spatial and temporal patterns suggest a role for vessels in neural cell development.

The functional relationships between neurons and blood vessels to ensure NVC mechanisms are only functional as of 3 weeks of age in rodents, and 7 to 8 weeks in humans [5, 21-23]. In the immature brain, the absence of NVC to neuronal activity pushes the brain to rely on alternative mechanisms for proper oxygen and nutrients supply [5]. Studies have suggested that an hypoxic state during early postnatal development is required, as maturation of the neuronal network utilizes energy for neurogenesis, synaptogenesis and maturation of astrocytes [7]. Thus, the increasing energy consumption as previously identified at the embryonic stage generates a

hypoxic environment, which will guide postnatal cerebrovascular development and remodeling [7]. For instance, hypoxia-inducible factor 1 (HIF-1) regulates the expression of angiogenic factors such as VEGF, angiopoietin-2 and placental growth factor [13]. Moreover, Dr. Lacoste made the discovery that neuronal activity drives brain angiogenesis during critical developmental periods after birth. Indeed, sensory inputs are necessary and sufficient to account for at least part of the very active cortical angiogenesis between postnatal day 0 (P0) and P30[24]

Moreover, the demand for a stable environment increases since the CNS requires a tightly controlled environment free of toxins and pathogens for proper chemical composition and synaptic transmission [25]. This is accomplished by the blood-brain barrier (BBB) which is uniquely found in the brain and characterized by specialized endothelial cells [26]. The BBB acts as a physical barrier where endothelial cells are sealed by tight and adherens junctions to restrict paracellular permeability [27]. In addition, specialized transporters such as glucose transporter GLUT1 and transferrin receptor CD71 control uptake of nutrients across the barrier, while pumping and receptor mechanisms dispose of toxic and waste products [27]. The endothelium is supported by a basement membrane enwrapped by pericytes, astrocytes and neuronal synapses [25, 28]. The lack of thereof, leads to a leaky (non-functional) BBB and possible onset of neurodegenerative diseases [29, 30].

As previously stated, one distinctive characteristic of cerebral blood vessels is the close interaction between endothelial cells, neurons and glial cells. This interaction allows for the regulation of blood flow in order to match metabolic needs [31]. As such, increased neuronal activity leads to a parallel increase in CBF [6]. Innervation of the cerebral cortex by projection neurons leads to the release of neurotransmitters (acetylcholine, noradrenaline, serotonin and glutamate) involved in the regulation of vessel diameter [32]. Intracerebral arterioles and

capillaries are similar in nature; however, they differ by the presence or absence of vascular smooth muscle cells (VSMCs) which are involved in regulating vessel tone [5, 28]. Intracerebral arterioles require VSMCs to control vessel tonicity as intracerebral capillaries are covered by pericytes which are embedded within the basal membrane [28]. These cells are required for proper vascularization and formation/maintenance of the BBB [25, 26, 29], but their involvement in NVC is matter of debate. Certain studies suggest that pericytes have contractile properties however, this is still debated [33]. In addition, astrocytes, which are closely related to the endothelium and cerebral synapses, can modulate the effect of neural activity. Their expression of glutamate receptors as well as their end-feet extensions sent around vessels can regulate VSMCs contraction and relaxation via release of astrocyte-derived vasomodulators (e.g. prostaglandins) [5]. Another glial cell in the brain consist of microglia which are involved in maintaining cerebral function and vascularization [34]. They act as macrophages however; studies suggest their involvement in vascular development during brain maturation [34].

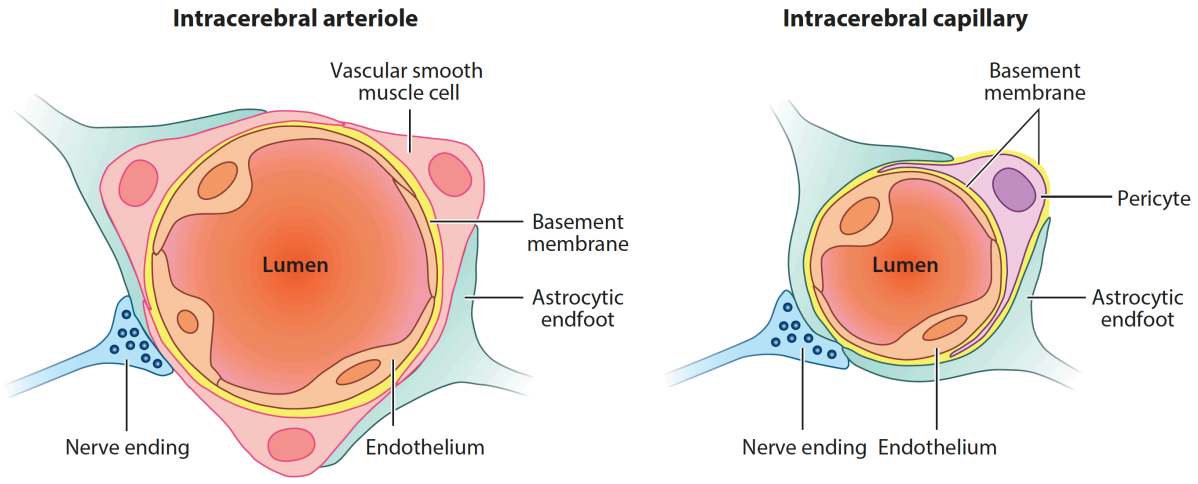

Figure 1. Schematic representation of the neurovascular unit.
Endothelial cells are surrounded by mural cells (astrocytes, pericytes, VSMCs) which are involved in maintaining the vascular integrity. Intracerebral arterioles (*left*) differ from intracerebral capillaries (*right*) by the presence of VSMCs to control vessel tone. Adapted from Andreone, Lacoste and Gu, 2015. *Annu Rev Neurosci* 38:25-46. With permission.

The important role of the brain vasculature in neural development suggest that deficits within the vascular system during this period will impact brain maturation and function. Moreover, the brain vasculature is considered a strong player in the onset of neurological diseases. For instance, any alterations in the vascular system during aging contribute to neurodegenerative diseases such as Alzheimer's disease, amyotrophic lateral sclerosis, and Huntington's disease, all of which have a demonstrated vascular aspect [35, 36]. Consequently, damaged or poorly developed cerebral blood vessels are known to lead to other morbid diagnostics.

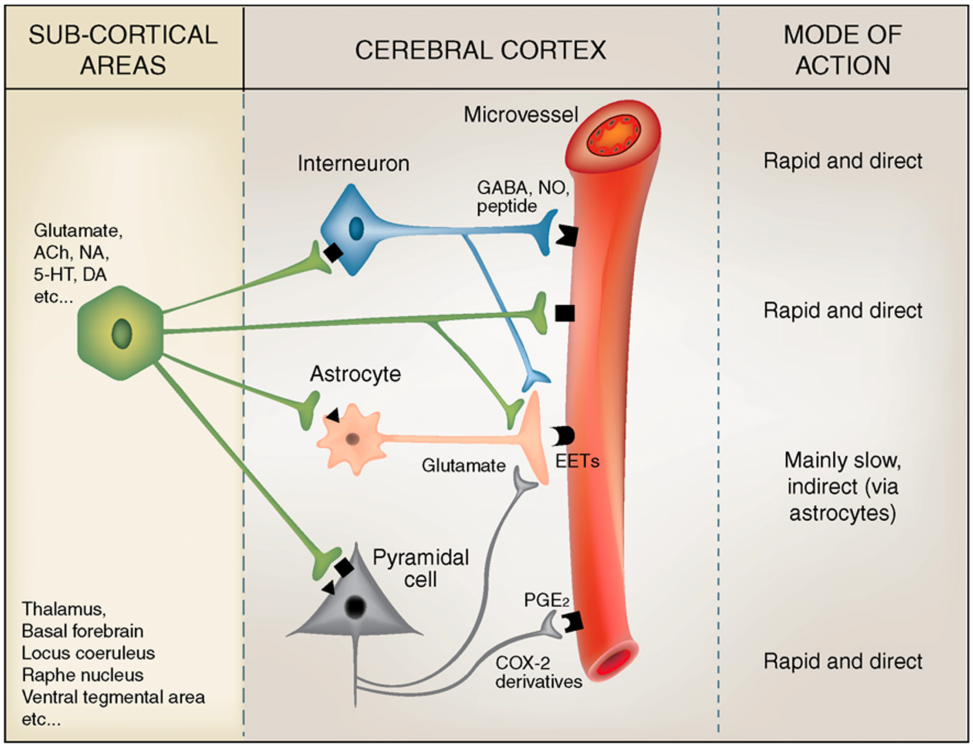

Figure 2. Regulation of cortical microvessels by neurons, interneurons and astrocytes. Neurons indirectly and directly interact with microvessels to modulate CBF. Indirect mode of action via astrocytes act as intermediaries to interneurons and pyramidal cells. Vasoactive mediators released from neurons and astrocytes can induce vasodilation or vasoconstriction responses. Adapted from Cauli and Hamel, 2010. Front Neuroenergetics 2(9):1-8. With permission.

1.2 Importance of the brain vasculature in health and disease

The brain vasculature plays a central role in the pathogenesis of several dreadful human diseases, as it is responsible for delivering oxygen and nutrients as well as maintaining a stable

environment [5]. Throughout development, adequate communication between the nervous and vascular system is required for proper brain function and maturation, as previously described [13, 31]. While endothelial cells are the building blocks of the brain vasculature, endothelial-based abnormalities are center-stage in relation to cerebrovascular disease, neurovascular injury and vascular factors in neurodegenerative diseases [37]. Findings on the onset of neurodegenerative disorders show CBF shortfalls and BBB dysfunction [7, 9, 38]. Studies have investigated vascular changes in animal models of neurodegeneration pertaining to neurovascular dysfunction, and in humans showing early CBF and BBB deficits that have been identified in neurodegenerative diseases [35] or diabetes-associated neuroinflammation [39].

Neurodegenerative diseases such as Alzheimer's disease (AD) have been extensively studied in rodent models showing classical pathological hallmarks (amyloid-β plaques, hyperphosphorylated tau neurofibrillary tangles, neuronal loss) [40]. Studies have been able to demonstrate that cerebrovascular pathology contributes to AD-associated dementia [41]. Neurovascular dysfunction is a primary event in AD progression [35]. For instance, CBF reductions, impaired cerebrovascular reactivity and impaired hemodynamic responses have been identified in early stages of AD [42]. In preclinical AD, CBF has been used as a biomarker for the disease since previous studies have revealed CBF reduction using arterial spin labeling magnetic resonance imaging (ASL-MRI) and positron emission tomography (PET) imaging [35, 43-45]. Neurovascular coupling responses are impaired in AD. For example, during visual stimuli there is a reduced CBF response as the BOLD signal (blood oxygen level dependent) is regionally altered [31, 46, 47]. This signal is able to provide local changes in deoxyhemoglobin content during neuronal activation [48]. Additionally, BBB breakdown has been identified in preclinical AD.

Individuals with early AD have an increase BBB permeability in the cortex, deep gray matter and white matter before the first appearance of dementia [49].

Furthermore, the brain vasculature has been implicated in other neurological disorders such as Parkinson's disease (PD), Huntington's disease (HD) and amyotrophic lateral sclerosis (ALS) [35]. Interestingly, decreased CBF has been identified in PD and HD patients. Most often, these deficits were revealed before cognitive dysfunction[38, 50]. ALS patients developed early perfusion deficits in the frontoparietal cortex, subcortical gray matter and white matter with the absence of cognitive decline[51]. Moreover, a dysfunctional BBB has been recognized in ALS. In a mouse model of ALS, they identified BBB breakdown, reduced tight junctions and expression of GLUT1 receptors. These defects were evidenced by leakiness of the blood-spinal cord barrier and preceded the onset of motoneuron degeneration [52]. Thus, animal models of neurodegenerative diseases have shown similar vascular deficits (BBB dysfunction and CBF reduction) which pertains to the importance of a well establish vascular network for proper CNS function [9, 38, 44, 52].

Apart from neurodegenerative disorders, experimental models of mural cell (VSMC, pericytes, astrocytes) and endothelial cell dysfunction have led to neuronal defects, as well as impaired CBF[7]. Vascular mural cell abnormalities can contribute to perfusion deficits. For example, dysregulation of transcription factors in VSMCs can alter arterial contractility and reduce CBF [7].

Cerebral autosomal-dominant arteriopathy with subcortical infarcts and leukoencephalopathy (CADASIL) is a disorder where abnormal VSMCs structure and function leads to cerebrovascular dysregulation. Both patients and rodent models of CADASIL demonstrate progressive subcortical ischemic injury [53].

In addition, progressive pericyte loss due to disruption of endothelial cell/pericyte communication coincides with BBB hyperpermeability after birth [29, 30]. BBB defects identified display an age-dependent impairment which develop a neurodegenerative-like phenotype (i.e. neuronal insults) with progressive cognitive deficits [7].

Considering these vascular functional deficits, we cannot disregard the importance/contribution of the blood vessels to a variety of neurological conditions as evidenced by the fact that vascular deficits can arrive prior to neural impairments. Thus, the commonality of vascular deficits in several neurological disorders and neurodevelopmental disorders demonstrate the importance of understanding the involvement of the brain vasculature in neurodevelopmental disorders, including ASD.

1.3. Autism spectrum disorders

Autism spectrum disorders (ASD) are neurodevelopmental disorders associated with social interaction deficits, communication impairments and repetitive behaviors. These disorders vary in symptom severity with children ranging from high functioning to severely impaired individuals requiring constant assistance [54]. Increase awareness and advancements in diagnostic/medical tools has led to a growing number of children being diagnosed with ASD [55, 56]. According to a report completed in 2015 by the National Autism Spectrum Disorder Surveillance System (NASS), 1 in 66 Canadian children and youths between 5-17 years old have been diagnosed with ASD (Public Health Agency of Canada, 2018). While males are four times more likely to be diagnosed with ASD when compared to females [54], the mechanisms leading to sex differences are unknown [57]. However, some theories have emerged suggesting that males are more vulnerable to genetic lesions and females require a bigger burden of genetic mutations and copy number variations (CNVs) to receive an ASD diagnosis [58, 59]. The NASS found that 1 in 42 males (23.9 per 1000)

and 1 in 165 females (6.0 per 1000) between the age of 5 -17 years old have ASD (Autism Spectrum Disorder among children and youth in Canada, NASS, Public Health Agency of Canada, 2018). Moreover, the increase awareness of these disorders has helped with finding methods for children in moderating ASD-related symptoms. Thus, children with ASD are able to attain a higher life expectancy. Consequently, more autistic children are entering adulthood, making ASD life-long disorders. However, with increasing life expectancies comes additional comorbid medical conditions such as seizures and cardiovascular diseases [55]. In general, the lifetime costs in Canada range from $1.2 million to $4.7 million for an individual on the autism spectrum [60]. Noteworthy, ASD not only affect patients but they also creates a burden on families and caregivers [61].

In order to receive an ASD diagnostic, individuals must present abnormal behaviors early in development. Diagnostic of these disorders are completed in two step: 1) developmental screening and 2) comprehensive diagnostic evaluation. In the first step, children are screened during regular doctor visits at 18 months and at 24 months where the pediatrician examines how the child learns, behaves and moves. If there is any sign of developmental delays, the child undergoes a second screening step by completing a comprehensive diagnostic evaluation which includes genetic and neurological testing, vision screening and other comprehensive medical tests [62] (Centers for Disease Control and Prevention, 2018). As of 2013, the American Psychiatric Association released the fifth edition of the Diagnostic and Statistical Manual of Mental Disorders (DSM-5), which is now the standard reference that healthcare providers use to diagnose ASD. In several cases, individuals with ASD show atypical behaviors associated with visual attention, imitation, social responses, motor control and reactivity by 12 months of age [56]. As well, it is difficult to distinguish children that are later diagnosed with ASD from typically developing

children before they are 1-year-old. By the age of 3, a child can be efficiently diagnosed with ASD as they show typical symptoms [56]. A child demonstrating three behavioral abnormalities including social interaction deficits, repetitive/stereotypical behaviors, and communication impairments [63] is more likely to receive a ASD diagnostic. Although children are diagnosed using similar behavioral categories, these disorders comprise a highly heterogeneous group of patients with complex developmentally-altered behaviors [63]. Currently, there are no treatments to treat ASD at their roots, or slow down their progression. However, there are methods to reduce debilitating symptoms such as aggression, self-injurious behaviors, agitation and hyperactivity. For instance, pharmacological treatments including antipsychotics, anticonvulsants, antidepressants and mood stabilizers can help moderate some of these symptoms. Furthermore, the high prevalence of comorbidities will determine the medication that can be given to individuals with ASD, thus adding to the difficulty of treating and managing the symptoms of these disorders [56]. In addition to the three behavioral categories previously discussed, children with ASD have reported intellectual disabilities, attention deficits, sensory sensibilities, obesity, metabolic disorders, gastrointestinal problems, immune deficits, anxiety and depression, as well as sleep disturbances [55, 64].

Despite the increase interest in understanding ASD, the causes are unknown. In the past decade, research has identified some neurobiological and genetic underpinnings associated with ASD [64]. Consequently, ASD have been associated with both environmental and genetic origins [54, 64]. There is evidence of the impact of environmental factors to the etiology of ASD, even with a predominant genetic influence [64]. For instance, several environmental risk factors have been taken into consideration to the contribution to ASD such as prenatal and post-natal factors which include exposure to teratogens, viral infections as well as autoimmune diseases, and hypoxia

[56].

In the first description of early infantile autism in 1943 by Leo Kanner, a child psychiatrist and physician, reports that these neurodevelopmental disorders have a biological/genetic component that eliminates the parental and environmental constituents as the sole contributors to ASD [65]. This statement refers to genetics being one of the main offenders in ASD etiology, which has led many studies to look into differently-expressed genes (DEGs) within these individuals. Since then, ASD are known as one the most heritable disorders where infants with high familial risk for ASD begin life with a 20% chance of developing ASD, compared to 1.5% in infants with low or unknown risk [61].

In individuals with ASD, gene defects and chromosomal anomalies have been found in 10-20% of individuals [56]. A large number of genes have been associated with ASD, some of which interfere with neurodevelopment *in utero* through childhood as well as in synaptogenesis and axon motility. For example, mutations in *Shank3*, *Syngap1*, *Synapsin*, *NCAM* and *MYO16* genes which are involved in synaptic function and axon motility can lead to an ASD diagnostic [66-70]. In consequence to these DEGs, studies have shown neurodevelopment structure and function abnormalities which dysregulates neural networks involved in socioemotional processing, a behavior commonly found in ASD patients, and abnormal brain structures and patterning. In most cases of ASD, children display an increase head size and body weight as well as cortical overgrowth [56, 61, 71, 72]. The increasing prevalence of ASD in the last decade has pushed studies to look in depth at the possible causes involved in its etiology.

1.4. Neuronal links to ASD

The majority of studies have focus on the neuronal contributions to the pathology of ASD. They have demonstrated that most patients have atypical neural activity with excessive local

connectivity within neural assemblies [73]. In 30% of cases, patients display abnormal electroencephalograms (EEG), with increased activity in most regions of the cerebral cortex [74]. Evidence supporting the ASD-related increased brain activity suggest that elevated cortical excitability correlates with altered expression of genes involved in GABAergic and glutamatergic neurotransmission systems. For instance, a reduction of GABA-related genes as well as lower counts of GABAergic neurons in ASD patients have been identified and accounts for increase excitability [75]. In addition, increased glutamate receptors and mRNA levels of glutamate-system-related genes (e.g. AMPA) have been reported in ASD [76]. Thus, the reduction of inhibitory signaling and higher expression of excitatory genes influence overall cortical activity in ASD. This excitability impacts neural synchronization, habituation and adaption, all of which can create disruptions in temporal processing, stimulus intensity coding, seizure susceptibility, and/or lead to sensory hyper- or hypo-sensitivity [77]. These changes are consistent with documented clinically-observed perceptual differences in ASD [77].

A recent study was able to make early predictions of ASD diagnosis by using functional connectivity MRI (fcMRI) data of 6-month-old infants with high familial risk for ASD. This study associated brain metrics with functional connectivity taken at 24 months of age, a time when these syndromes can be diagnosed by ASD-related behaviors [61]. Brain metrics measured in fcMRI showed a relationship between functional connectivity and ASD-related behaviors. Test for social communication, cognitive abilities and repetitive behaviors displayed altered brain functional organization in children with ASD at 24 months of age [61].

In addition to abnormal cortical activity, a study demonstrated an overproduction of neurons in ASD patients. Neuronal numbers were counted in typically-developing children as well as ASD children. They identified 67% more neurons in the prefrontal cortex in ASD children when

compared to typically developing children [78, 79]. Not only does an increase in neuronal numbers affect overall function, but it also leads to structural changes. Brain overgrowth and excess neurons in the neocortex have been shown in 20% of children with ASD. Furthermore, studies revealed an elevated neural density and number in ASD patients [80]. In order to study this avenue, one report generated a mouse model consisting of an overproduction of excitatory neurons in neocortical layer 2/3 [81]. This model displayed abnormal neuronal morphology as well as ASD-like behaviors, such as deficits in social interactions and compulsive/repetitive behaviors [81].

Although several studies have shown an increase in neuronal production, ASD patients also demonstrate altered synaptic connections. For instance, there is an excess synaptic protein synthesis and a reduced synaptic pruning [82]. The balance between these two mechanisms are altered in ASD patients, which contributes to developmental deficits identified in these patients [82].

While studies have shown great interest in the neuronal contribution to the ASD pathophysiology, very little attention has been drawn to the vascular system, even if both neural and vascular systems are anatomically closely tied to each other, and are co-dependent to establish correct connectivity and wiring. In this thesis, I will expose our overarching hypothesis that an impaired vascular system may contribute to the pathophysiology of ASD.

1.5. Vascular links to ASD

In a typically-developing brain, blood vessels are stable and can continuously delivery nutrients and growth factors for normal maturation and function [5]. Very few studies have looked at the involvement of blood vessels on neurodevelopmental disorders. So far, the majority of studies have concentrated on fMRI and single photon emission tomography (SPECT) analysis of ASD brains and have identified altered perfusion in different regions [31, 83].

As ASD have a very complex nature, patients with these disorders demonstrate variable perfusion abnormalities in different areas of the brain [83, 84]. This variability can be attributed to the heterogeneity of etiological factors and symptoms found in ASD patient cohorts [85]. Considering, the age gap of patients (28 months to 37 years old), the different comorbid diseases and varying behavioral deficits, studies were able to identify comparable perfusion rates as the main finding in patients with ASD [85, 86]. Consequently, ASD patients demonstrated hyperperfusion in the frontotemporal cortex, while hypoperfusion was identified in other regions of the brain [85]. In most cases, prefrontal areas and temporal regions were the most affected by altered perfusion [83, 87-93]. Other studies have focused on metabolic requirements of ASD patients in which, most often, CBF monitoring served as a surrogate for metabolic activity. This suggests that the identified frontotemporal hyperperfusion is indicative of hypermetabolism in ASD [85]. Considering that blood vessels are required to provide oxygen, glucose and nutrients to the brain via the blood stream to maintain supply, studies have yet to identify if the vascular deficits are impacting neuronal function, and/or if altered neuronal function leads to cerebrovascular defects [83]. Hence the importance to understand the involvement of cerebral blood vessels in ASD pathogenesis and/or progression.

Furthermore, studies were able to correlate ASD-like behaviors to regional cerebral blood flow (rCBF). One study used SPECT to measure rCBF in patients with infantile autism and compared its data to a group of healthy control subjects [91]. This resulted in abnormal rCBF in the frontal cortex, temporal cortex and hippocampus of ASD patients. Moreover, this study reported correlative relationships between these results and symptom profiles [89]. CBF abnormalities seemed to correlate with cognitive dysfunction in ASD children [61]. It was suggested that perfusion patterns suggest possible locations for abnormalities in brain function

underlying ASD-like behaviors [94].

Although research has focused on CBF, only one study approached the link between angiogenesis and ASD. This study was completed using postmortem brain tissue from severely affected patients who died from complications associated with ASD. Authors suggested that angiogenesis is active for a longer period of time in ASD children and young adults ranging from 2.8-28 years old [71]. Nonetheless, this study focused primarily on cells surrounding vessels (i.e. increased pericyte proliferation) and did not provide a thorough descriptive and mechanistic investigation on relationships between the vascular networks and ASD pathogenesis.

Another study demonstrated that a mutation in an amino acid transporter found at the BBB was able to lead to ASD-related behaviors. This work published in *Cell* identified a mutation in the large neutral amino acid transporter (LAT1) present at the BBB. Mice with mutant LAT1 demonstrated ASD-like behaviors, including reduced explorative behavior, locomotion impairments and social deficits in a three-chamber test [95]. Administration of the missing amino acids rescued some of the impaired behaviors [95]. Although this studies did not specifically investigate the cerebrovascular contribution to ASD in terms of development, the authors were able to demonstrate an aspect of altered vasculature.

Despite these interesting findings, none of the above-mentioned studies have investigated a possible link between altered cerebrovascular development and ASD pathogenesis. Hence, more research is required at the system, cellular and molecular levels to fully understand this connection. The overarching hypothesis we tested in the study presented here is that **pathological development of the brain vasculature represents a structural and functional determinant in ASD pathophysiology.**

1.6. 16p11.2 deletion syndrome

Both single gene and chromosomal mutations have been linked to ASD diagnostic. Chromosomal microarray analysis is a widely-used method to identify missing or extra chromosome fragments [96]. This detection method has led to an increased identification of recurrent genomic anomalies including deletions and duplications at chromosome 1q21.1, 15q11-13, 22q11-13 and 16p11.2 [97]. These genomic anomalies are also known as copy number variations (CNVs), and accumulating evidence from ASD research supports the importance of CNVs[98-100]. The focus of this thesis is on the 16p11.2 deletion, one of the most common genetic causes of ASD [96, 101]. Indeed, CNVs associated with mental illnesses are found at significant frequency in the human 16p11.2 locus [102-105]. While 16p11.2 microduplications are risk factors for schizophrenia [106-108], reciprocal microdeletions are common etiological factors in ASD patients [105, 109, 110] and children with mental retardation[111, 112]. Approximately 2% of all patients with ASD possess a 16p11.2 microdeletion [96, 113, 114]. Although this deletion can be inherited, 75% of cases are *de novo* (16p11.2 Deletion Syndrome Guidebook, Simons VIP Connect, 2015)[115]. Among the highly-conserved genes found in the human 16p11.2 locus, several genes control critical features of brain development and neuronal function. For instance, *Mvp* or *Yelp3* control cell cycle progression, cellular motility, proliferation, differentiation or senescence [116-118]. In addition, *Taok2* or *Kctd13* regulate neuronal differentiation and maturation [119-123], while *Doc2A* and *Prrt2* control synaptic transmission and neuronal excitability [124-128].

ASD-related behaviors have been associated with the 16p11.2 deletion such as repetitive/restrictive behaviors, difficulties with social interactions and communication skills [63]. Furthermore, children harboring this deletion have developmental problems such as difficulties

with learning, understanding as well as speech and language deficits (71%) [129, 130]. In most cases, children struggle with receptive/expressive language as well as phonological difficulties [130]. In addition, 53% of 16p11.2 deletion children have developmental coordination disorders where parents often describe their child as being clumsy (16p11.2 Deletion Syndrome Guidebook, Simons VIP Connect, 2015). These characteristics are one of the first signs the parents notice during their child development. In a study completed in 2010, hypotonia, gross motor, or fine motor delays were identified in 57% of patients in addition to emotional out-bursts (29%), attention issues (14%) and sleep difficulties (10%) [96]. Notably, 16p11.2 deletion patients have altered growth patterns, larger than average head size and increase neurological issues such as seizures and epilepsy [55]. While children display ASD-related characteristics they can be associated with other medical complications such as gastrointestinal problems, ear infections (36%), scoliosis (10%), and congenital heart disease (6%) (16p11.2 Deletion Syndrome Guidebook, Simons VIP Connect, 2015) [55, 131]. Structurally, children with this deletion display a widespread of alterations in brain white matter microstructure compared with typically developing children [132]. Additionally, abnormally thick cortex in the left lateral temporal and mesial occipitoparietal regions as well as a thick corpus callosum were evidenced in ASD patients [114, 133]. These altered structural and behavioral characteristics in 16p11.2 deletion patients further confirms this mutations involvement in ASD.

Important to the context of this thesis are 16p11.2 genes expressed in endothelial cells [134] and directly or indirectly modulating angiogenesis. Numerous studies have linked *MapK3* to angiogenesis, as its product ERK1 signals downstream of the vascular endothelial growth factor (VEGF) receptor 2 (VEGFR2) to regulate EC proliferation and migration [135-139]. The genes *Tmem219* and *Coro1A* negatively modulates EC apoptosis[140] while *Maz1* potentiates VEGF-

induced angiogenesis [141, 142]. Altogether, these findings prompted us to test our idea of a compromised brain vasculature in ASD using a validated mouse model of the 16p11.2 deletion syndrome.

Interestingly, it is possible to study the 16p11.2 deletion syndrome at the preclinical level in animal models. In particular, the 16p11.2 locus is highly-conserved in the syntenic 7qF3 region in mice, thus making it possible to accurately replicate the deletion in a rodent model [143-145]. Although no rodent model can perfectly encompass all aspects of ASD, the 16p11.2 deletion mouse model is representative of a significant population of individuals with ASD. Furthermore, it displays several ASD-related characteristics which are fundamental for a diagnostic. This model makes it ideal to study different aspect in these disorders. Using this model, we will investigate the vascular contributions to the ASD pathophysiology (see section 1.8).

1.7. Objective and Hypothesis

ASD are mostly studied from a neuronal point view. Yet, research has demonstrated functional cerebrovascular abnormalities in ASD patients. However, no studies have looked in depth at the cerebrovascular involvement to these disorders. This novel vascular angle will reveal new players involved in ASD pathogenesis as well as identify new targets for developing transformative therapeutic strategies to better the quality of life of an individual with ASD.

The objective of this thesis was to investigate the pathological development of the brain vasculature in an ASD mouse model. We hypothesize that the ***pathological development of the brain vasculature represents a structural and functional determinant in ASD pathophysiology.*** This overarching hypothesis will be addressed by the following three objectives:

Objective 1: Examine the health of the brain vasculature in a genetically-engineered mouse model that possesses a human mutation specifically linked to ASD.

Objective 2: Determine the cellular and molecular mechanisms underlying ASD- associated brain endothelial deficits.

Objective 3: Investigate the endothelial contribution to ASD-related phenotypes using a conditional, cell-specific genetic approach.

1.8. Model systems to investigate 16p11.2 deletion associated cerebrovascular deficits

To test our overarching hypothesis that cerebrovascular deficits play a critical role in ASD, this thesis is centered around the use of *16p11.2*$^{df/+}$mice [143] and *16p11.2*$^{flox/+}$ mice [144].

Heterozygous *16p11.2*$^{df/+}$ mice possess a deletion on chromosome 7 spanning 440kb containing 30 genes [143]. The murine deletion encompasses the same genes and sequence found on chromosome 16 in humans. This model displays behavioral as well as structural abnormalities that are commonly found in patients with this deletion. For instance, these mice show hyperactivity and male-specific sleep deficits [146], problems in habituating to new environments [143], stereotypic behaviors [143, 145], recognition memory deficits [144, 145] and movement control difficulties [144]. In addition, adult males harboring the 16p11.2 deletion display reduced social interactions and ultrasonic vocalization during interaction with a female [147]. Structurally, these mice demonstrate an increase in brain volume in the basal forebrain, superior colliculus, fornix and midbrain [143]. Noteworthy, these mice have a low body weight and exhibit normal general health and neurological reflexes, as well as increased expression of transmitter receptors (glutamate receptor mGluR5 and dopamine receptors D1 and D2) together with electrophysiological defects in the striatum and prefrontal cortex [143, 144, 148]. Our focus will be on the brain vasculature of *16p11.2*$^{df/+}$and their WT littermates, with special attention to the cerebral cortex.

To perform Objectives 1 and 2, we will use *16p11.2*$^{df/+}$ mice (purchased from Jackson and bred in-house) to assess the effects of constitutive 16p11.2 haploinsufficiency on the brain vasculature during development at the physiological, anatomical and cellular levels (*in vivo*, *ex vivo*, and *in vitro*).

To perform Objective 3, we will achieve endothelial-specific 16p11.2 deletion using the Cre/Lox system. Our breeding strategy allows for excision of the LoxP-flanked 7qF3 locus (*16p11.2*$^{flox/+}$; Jackson) on one allele, following Cre-mediated recombination under the control of endothelial promoter *Cdh5* (*Cdh5-Cre*$^{tg/+}$; Jackson; CRE active from embryonic day 8)[149]. In *Cdh5-Cre*$^{tg/+}$*;16p11.2*$^{flox/+}$ mice, 16p11.2 haploinsufficiency is induced in endothelial cells only to assess impacts of the vascular mutation on angiogenesis and surrounding neurons.

2. Materials and Methods

2.1. Animals

All animal procedures were approved by the University of Ottawa Animal Care Committee and were conducted in accordance to guidelines of the Canadian Council on Animal Care.

Mouse husbandry. All mice were bred in house and housed maximum five per cage with free access to water and food. Males *16p11.2*$^{df/+}$ (Jackson laboratory, stock #013128[150]; mixed B6/129 background) were crossed with WT females of the same background (Jackson laboratory, stock #101043) to obtain hemizygous *16p11.2*$^{df/+}$ offspring as well as WT littermates. Conditional *Cdh5-Cre*$^{tg/+}$;*16p11.2*$^{flox/+}$ mutants (i.e. '*16p11.2*^{Vasc}'; mixed B6/129 background) and littermate controls were obtained from breeding between *Cdh5-Cre*$^{tg/+}$ males (Jackson laboratory, stock #006137, B6 background) and *16p11.2*$^{flox/+}$ females (Jackson laboratory, stock #025330 [144]; 129 background). As recommended by Jackson Laboratory to improve *16p11.2*$^{df/+}$ pup survival, breeding cages (both constitutive and conditional mutants) were supplemented with breeding chow

(#2019, Envigo Teklad) and DietGel (#76A, ClearH_2O) up to weaning age. To assess astrocyte coverage/number in 16p11.2 hemizygous mice, *16p11.2*$^{df/+}$ males were crossed with *Aldh1l1-eGFP* (BAC) females (Jackson laboratory, stock #026033; B6 background).

Genotyping. 16p11.2$^{df/+}$ mice and WT littermates were genotyped using the two following primers: 5'-CCTCATGGACTAATTATGGAC-3' (forward) and 5'-CCAGTTTCACTAATGACACA-3' (reverse) with a PCR product of 2.2Kb for *16p11.2*$^{df/+}$ mice[150]. Conditional *16p11.2*^{Vasc} mutants (*Cdh5-Cre*$^{tg/+}$;*16p11.2*$^{flox/+}$) were genotyped as follows: For *16p11.2*$^{flox/+}$ genotyping[144], three primers were used: 5'-TTCGGCTTCTGGCGTGTGAC-3' (p26, forward), 5'-TTGGACAGACCCTGGTTCAGTC-3' (p301, forward) and 5'-GGTGGATGTGGAATGTGTGCGAG-3' (p132, reverse), with two PCR products of 431bp and 341bp. For Cre genotyping, primers used were: 5'-GCAAGTTGAATAACCGGAAATGGTT-3' (forward) and 5'-AGGGTGTTATAAGCAATCCCCAGAA-3' (reverse), with a 250bp PCR product. For *Aldh1l1-eGFP* genotyping, primers were: 5'-GAACAGGCGAAAGCGTTAAG-3' (23136, forward), 5'-GTAAACCTCCTGGCCAAACA-3' (18707, reverse), 5'-CTAGGCCACAGAATTGAAAGATCT-3' (oIMR7338, forward), and 5'-GTAGGTGGAAATTCTAGCATCATCC-3' (oIMR7339, reverse) with PCR products of 550bp (transgene) and 324bp (internal positive control).

2.2. Photoacoustic imaging

Imaging was performed using the Vevo LAZR-X high-frequency ultrasound and photoacoustic (PA) imaging system (FUJIFILM VisualSonics, Toronto, Canada). All images were acquired using the MX250 21MHz linear array transducer, fitted with medium sized optical fibers. Animals were anesthetized with a xylazine/ketamine cocktail (0.1 ml/100 g). The head of each animals was secured and stabilized using a stereotactic frame attached to the imaging platform. Key

physiological parameter such as heart rate, respiration rate and temperature were monitored throughout the imaging session. B-mode imaging was used for region of interest selection, followed by PA and contrast mode. 2D and 3D PA images were acquired under Oxy-Hemo Mode, using dual-wavelength imaging, alternating between 750nm and 850nm, for real-time display of oxygen saturation (sO_2). For contrast imaging, a 27G butterfly needle was inserted into a lateral tail vein for intravenous injection of the MicroMarker (FUJIFILM VisualSonics, Toronto, Canada) contrast agents. Contrast enhanced images were collected after a 50µL bolus injection of MicroMarker using non-linear contrast imaging. All 3D data were acquired by moving the transducer with a stepper motor, at a step size of 254µm.

2.3. Laser Doppler flowmetry

Laser Doppler flowmetry measurements of evoked cerebral blood flow (CBF) in response to sensory stimulation were carried out as previously described (Lacoste *et al.* 2013[151]). CBF was recorded over the contralateral somatosensory cortex before, during and after unilateral stimulation of the right whiskers with an electric tooth brush (20 sec at 8 to 10 Hz). Six recordings were acquired every 60 sec and averaged for each mouse. Quantifications of hemodynamic parameters (e.g. baseline CBF, %CBF increase from baseline, rising slope, time to maximum response, falling slope) were inspired from Chen *et al.* 2011[152].

2.4. Cardiovascular monitoring

Systolic blood pressure and heart rate were measured by tail-cuff plethysmography (Visitech BP-2000, Apex, NC). Mice were trained for 5 consecutive days prior to the actual recordings for 5 days. Measurements were acquired each day (5 preliminary readings followed by 10 recordings) at fixed time. The 5-day average of systolic blood pressure and heart rate was then calculated.

2.5. Pressure myography

Compounds. Adenosine, acetylcholine (ACh), phenylephrine (PE), sodium nitroprusside (SNP) and L-N^G-Nitroarginine (L-NNA) were purchased from Sigma-Aldrich. Compounds for Kreb's solution were purchased from Sigma-Aldrich (MgSO4, KH2PO4, NaHCO3 and glucose) or Fisher Chemical (CaCl2, NaCl and KCl).

Procedure. Mice were decapitated and the brains were immediately immersed in cold (4ºC) oxygenated (5% CO2) Krebs' buffer solution (37± 0.5ºC, pH 7.4 ± 0.1) containing (in mM): 118 NaCl, 4.5 KCl, 2.5 CaCl2, 1 MgSO4, 1KH2PO4, 25 NaHCO3, and 6 glucose. As described previously in (Tong et al. 2005), segments (~2 mm long) of the middle or posterior cerebral arteries were carefully dissected and cannulated with a glass pipette (~40μM diameter) at one end and sealed to another glass pipette on the other end. Intraluminal pressure was maintained at 60 mmHg using a pressure- servo controller (PS-200) (Living Systems Instrumentation). Vessels were superfused (6 ml/min) with oxygenated Krebs' solution in a chamber for online videomicroscopy. All compounds were applied extraluminally and changes in lumen diameter was measured using a closed-circuit video system (National Electronics, Taiwan). Dilatory responses to adenosine (10^{-10} to 10^{-4} mol/L), acetylcholine (ACh, 10^{-10} to 10^{-5} mol/L) and sodium nitroprusside (SNP, 10^{-10} to 10^{-4} mol/L) were tested on vessels pre-constricted submaximally with phenylephrine (PE, $2X10^{-7}$ mol/L). Contractile responses to PE (10^{-9} to 10^{-4} mol/L), and the tonic production of the vasodilator nitric oxide (NO) were measured in vessels at basal tone, the latter after inhibition of NO synthase (NOS) with Nω-nitro-L-arginine (L-NNA, 10^{-5} mol/L, 40 minutes).

Analysis. Dose-response curves were generated as percentage of changes from pre-constricted tone (vasodilators) or basal tone (PE and L-NNA). Percentages of change were plotted as a function of agonist concentration or incubation time (L-NNA).

2.6. Wire myography

Mesenteric arteries isolated from both WT and 16p11.2$^{df/+}$ mice were used to assess peripheral vascular reactivity *ex vivo* as previously described (Thibodeau *et al.* 2016[153]). Briefly, second order branches were obtained, and were carefully cleaned of adipose and connective tissue. Segments (~ 2 mm) were mounted on a Multi-Wire Myograph System (DMT) and equilibrated in Krebs solution with 95% O_2 and 5% CO_2. Vasoconstriction or endothelium-dependent vasorelaxation were examined in response to PE or Ach (1nM- 10μM), respectively.

2.7. FDG-PET scan

Mice were fasted for 8 hrs prior to imaging, and anesthetized by isoflurane. A tail vein cannula was inserted prior to being placed in a custom 4-position multi-animal hotel secured to the gantry of an Inveon D-PET scanner (Siemens). Mice were kept warm during the duration of the PET scan, which was followed by a 10 min transmission scan acquired under standard conditions. Once aligned in the PET field of view, a 45-minute acquisition protocol in list mode format was initiated and approximately 200 μCi [^{18}F]-4 fluoro-D-deoxyglucose (FDG) was injected intravenously exactly 30 sec afterwards. Iterative reconstruction was performed using 3D ordered-subsets expectation maximization (3D-OSEM) followed by fast maximum *a posteriori* (fastMAP) with the following parameters: MAP OSEM iterations, 2; MAP subsets, 16; MAP iterations, 18. Under anesthesia, mice were immediately transferred to a 3.0 T pre-clinical MRI (MR Solutions Inc.), and a T_2-weighted, axially sectioned, respiratory-gated Fast Spin Echo image of the head was acquired with the following parameters: 31 slices; 0.5 thickness and 0.1 spacing; FOV = 30 with FOV ratio = 0.75; TR=4800, TE=68, nex=4. VivoQuant (v. 4.0., InviCRO) was used for visualization of radiotracer uptake in the brain, to align PET with MRI images, and to segment the brain into individual brain regions using a proprietary mouse brain atlas algorithm. The count

densities were averaged for all volumes of interest at each time point to obtain a time *versus* activity curve for the entire brain, and average count densities were averaged for each brain region analysed for a bin spanning 40 to 45 min post-FDG injection. All quantified data were normalized to injected dose, measured by a CRC-15 PET dose calibrator (Capintec Inc), and expressed as percentage injected dose per mL of tissue (%I.D./mL).

For *in situ* autoradiography, fasted mice were administered 500 μCi of FDG by intravenous bolus injection under isoflurane anesthesia, followed by euthanasia by exsanguination *via* cardiac puncture 45 min after radiotracer injection. Cardiac perfusion was performed with saline to clear blood from tissues, and brains were resected and frozen in optimal cutting temperature medium compound (Tissue-Tek) on dry ice. Frozen blocks were equilibrated to -20°C for 30 min prior to sectioning. Tissue 12 μm-thick sections were mounted onto microscope slides, air dried for 5 min, and exposed to a [^{18}F]-sensitive storage phosphor screen (Perkin Elmer) overnight at 4°C. Screens were scanned on a Cyclone Storage Phosphor System (Perkin Elmer), and image data was processed with ImageJ.

2.8. Immunohistochemistry (IHC)

For IHC experiments, all mice were euthanized by cervical dislocation. Whole brains or dissected cortices were fixed in 4% paraformaldehyde (PFA) overnight at 4ºC. For 2D imaging experiments, following fixation, all brains were rinsed in PBS, submerged in 15% sucrose overnight, followed by 30% sucrose overnight, then embedded in OCT and cut coronally into 25μm-thick serial sections using a cryostat (HM525 NX, Thermoscientific), and finally mounted on charged glass slides. For 3D vascular reconstructions, flatten cortices were embedded in agarose and cut tangentially into serial 120μm-thick sections with a vibratome (VT1000S, Leica) and processed free-floating. Sections were blocked using a solution containing 10% donkey serum, 0.5% Triton

X-100 in PBS (0.5%PBT) and 0.5% cold water fish skin gelatin, and incubated overnight at room temperature (RT) with combinations of primary antibodies including anti-CD31 (1:200, BD pharmingen), -VGLUT2 (1:500, Cedarlane), -IBA1 (1:1000, Cedarlane), -PDGFR-ß (1:200, Cedarlane), -αSMA (1:200, Abcam), -GFP (1:500, Invitrogen), -VEGFR2 (1:500, R&D systems) or -mCherry (1:500, Abcam). On the next day, sections were washed with 0.5% PBT and incubated with species-specific AlexaFluor secondary antibodies (1:300, Invitrogen) for 3 hours at RT. Sections were washed with 0.5% PBT and PB (floating sections mounted) then coverslipped in Fluoromount G (EMS).

2.9. Image acquisition

Immunostained sections were examined under a Zeiss Axio Imager M2 microscope equipped with a digital camera (Axiocam 506 mono) as well as the Zeiss ApoTome.2 module for optical sectioning. For 3D reconstruction of vascular networks, tangential cortical sections comprising barrel cortex layer IV were used as a landmark: layer IV was located with VGlut2-immunofluorescent barrels under a 5X objective, then 60 µm deep z-stacks were acquired at 10X in three major subdivisions of the flattened cortex (anterior, parietal, occipital) for thorough sampling and representation of cerebral cortex. Tangential sections above and below layer IV were considered as layer II/III and V, respectively, as described previously[24]. For 2D imaging, a 10X or 20X objective was used to acquire 20 µm (10X) or 15 µm (20X) deep z-stacks that were subsequently transformed into maximal intensity projection images for quantifications (see below).

2.10. Computational morphometric analysis of 3D vascular images

Computational image analysis was performed as previously described[24]. In brief, a Gaussian smoothing filter with unit standard deviation was applied to each 3D image. Then, a circular-

window adaptive threshold with a radius of 36 microns was used to binarize the images. Connected components with volume smaller than 375 microns were removed from the image. The Palágyi-Kuba thinning algorithm was used to calculate the medial lines of the blood vessels, which were then represented as a graph. Each termination and bifurcation of a blood vessel becomes a node, and nodes are connected whether there is a blood vessel segment between them. The length of each blood vessel segment was calculated, and segments shorter than 9 microns were removed. The blood vessel density in the stack was calculated as the sum of the lengths of all blood vessel segments divided by the volume of the stack. The number of bifurcation nodes was also calculated. Please refer to Lacoste *et al.* 2014[24] for a more complete description of this methodology. The tortuosity was calculated as follows. For each voxel in the medial line of a blood vessel segment, henceforth called the reference voxel, all voxels having a Euclidean distance smaller than 18.15 microns from the reference voxel were selected. Such voxels, which include the reference voxel, are the local neighbors of the reference voxel. Then, a straight line was adjusted to the set of local neighbors by using least squares regression. The average point to line distance between the local neighbor voxels and the adjusted straight line defined the tortuosity of the blood vessel at the position of the reference voxel. The overall tortuosity associated to a stack was calculated as the average tortuosity of all blood vessel voxels in the stack.

2.11. Quantification of VSMC, pericytes, astrocytes and microglia coverage/number on 2D images

For cellular coverage quantifications (VSMCs, astrocytes, microglia, pericytes), a 10X objective was used, while a 20X objective was used for counting DAPI-counterstained cell bodies. Image analysis was completed with Fiji-ImageJ. Coverage was determined by converting the image to 8-bit, running *Z-Project* with the *Max Intensity* setting to obtain a 2D image. Image threshold was

determined with the Moments pre-set to acquire a binary image. *Analyze Particles*, with size set to 5-infinity, was used to find the proportion of the image containing the signal of interest. Pericyte coverage of cortical vessels was quantified by analyzing the proportion of total CD31-positive endothelial surface area also positive for the pericyte marker PDGFR-β. For cellular coverage by glial cells, the cortical area occupied by IBA1- or eGFP(ALDH1L1)-positive cells was quantified as surface occupied by labeling within the image. For artery quantification, the proportion of CD31/α-SMA-double positive cortical vessels was quantified. Number of cell bodies (pericytes, microglia, astrocytes) were manually counted using the *Cell Counter* plugin. For each animal 9 images were used (3 images per section, 3 sections). All data were expressed as percent of controls.

2.12. Transmission electron microscopy (TEM)

Mice were anesthetized with a mix of ketamine and xylazine (1mg/kg, intraperitoneally) and perfused through the aortic arch with 3.5% acrolein and 4% paraformaldehyde. Fifty-micrometer-thick coronal sections of the brains were cut in sodium phosphate buffer (PBS 50 mM, pH7.4) using a Leica VT1000S vibratome (Leica Biosystems) and stored at -20^{o}C in cryoprotectant until further processing (Tremblay *et al.* 2010[154]). Sections were post-fixed and embedded using variations of the protocol by Deerinck et al. (https://ncmir.ucsd.edu/sbem-protocol). In brief, the sections were washed 3 times in PBS for 10 min, and were incubated in 1.5% potassium ferrocyanide and 2% aqueous osmium tetroxide in 0.1M phosphate buffer (pH 7.4) for 1 hour at room temperature. The sections were subsequently washed 5 times with double-distilled water (ddH_2O) for 3 minutes, then incubated 20 minutes in a fresh solution of thiocarbohydrazide (1% w/v) at room temperature. Sections were washed again 5 times with ddH_2O for 3 minutes, incubated 30 minutes in 2% aqueous osmium tetroxide, and washed 5 times with ddH_2O for 3 minutes. Sections were dehydrated using increasing ethanol concentrations followed by propylene

oxide, and then embedded in Durcupan resin (Sigma-Aldrich) between ACLAR sheets at 55°C for 3 days, as described previously (Bisht *et al.* 2016,[155]). Ultrathin sections were generated at ~65 nm using a Leica UC7 ultramicrotome. Imaging was performed in the antero-frontal (2.8 to 1.98mm Bregma) and parieto-somatosensory (-0.70 to -1.82mm Bregma) areas. In each region, 10 capillaries per animal, ranging in diameter between 3 and 6 μm, were randomly photographed, using a FEI Tecnai Spirit G2 transmission electron microscope operating at 80kV and equipped with a Hamamatsu ORCA-HR digital camera (10 MP). For each capillary, an image at 4800X was acquired, in addition to 1-3 images at 13000X to generate a high-resolution mosaic of the capillary.

2.13. TEM image analysis

Quantifications were completed using the Fiji-Image J. The averaged diameter of the vessel lumen was calculated using the *Line tool* in both horizontal and vertical orientations. To analyze astrocyte endfeet, a region of interest was drawn around each astrocyte endfoot in contact with the blood vessel. The *Measure* function was used to calculate the area of the each endfoot. For each image, the total endfoot number in contact with the vessel was tallied, as was the combined area of all endfeet.

2.14. Endothelial cell isolation

All mice were euthanized by cervical dislocation. Cell isolations were completed following the manufacturer's instructions. The cortex was dissected in cold HBSS (without calcium and magnesium) using tools that were submerged in 100% ethanol for 30minutes prior to dissection. Cortical tissue was minced and incubated in Neural Tissue Dissociation compounds (Kit P, Miltenyi Biotec) to obtain a cell suspension.

For cell cultures. Cortical ECs (cECs) were isolated by incubation with CD31-coated magnetic

microbeads (130-097-418, Miltenyi Biotec) and placed in the magnetic MACS separator for positive selection. To obtain a pure endothelial cell population, cECs were cultured in an endothelial cell culture medium (MV2, PromoCell) replaced 24hrs post-seeding and every 48hrs until appropriate level of confluence is reached (30-40% for ICC; 90-100% for matrigel experiments).

For RNA isolation. ECs were isolated as above, but with additional steps to deplete myelin (Myelin removal beads II, Miltenyi Biotec) and CD45-positive cells (CD45 microbeads, 130-052-301, Miltenyi Biotec) to obtain a pure CD31-positive cell suspension. Cell suspensions from two animals were pooled in one biological replicate. RNA was acutely extracted using this suspension (E.Z.N.A. HP Total RNA kit, OMEGA bio-tek), with additional DNase step (E1091, OMEGA bio-tek) following the manufacturer's protocol. (RNA quality and purity (OD260/280 ratio, RQN) were measured using a bioanalyzer, and RNA samples passing quality standards (OD260/280 between 1.8 and 2, RQN > 9) were used for RT-qPCR.

2.15. Immunocytochemistry (ICC)

ECs were cultured on a cover glass for subsequent mounting for microscopy. Prior to staining, cells are washed twice in pre-warmed PBS and fixed for 10 min in cold 4% PFA. Fixed cells were permeabilized in a blocking solution containing 10% donkey serum, 0.1% Triton X-100 in PBS (0.1% PBT) and 0.5% cold water fish skin gelatin. Primary antibodies anti-CD31 (1:200, BD pharmingen) and -VE-Cadherin (1:500, Fisher Scientific) were diluted in blocking solution and incubated for 2 hours at RT. Cells are rinsed with 0.2% PBT. AlexaFluor species-specific secondary antibodies were diluted in blocking solution and incubated with cells for 60 min. Cells were washed with 0.2% PBT then 0.1M PB. Cover glass with stained ECs were mounted on slides in Fluoromount G and imaged (40X objective) with a Zeiss Axio Imager M2 microscope equipped

with a digital camera and ApoTome.2 module.

2.16. Cell cycle analysis

Endothelial cell suspensions were pelleted at 1000 g for 5 minutes and resuspended, then fixed in increasing concentrations of ethanol (up to 70%) for 60 minutes at 4 ºC. Fixed cells were pelleted at 1000 g for 10 minutes and resuspended in a Krishian buffer (0.1% sodium citrate, 0.02 mg/ml RNAse A, 0.3% NP-40 and 0.05 mg/mL propidium iodide). Cells were pelleted again and incubated in fresh Krishian buffer for another 60 minutes on ice in the dark. Finally, cell suspensions were filtered using a 25G needle and analyzed for propidium iodide labeling of DNA by flow cytometry (LSR Fortessa).

2.17. *In vitro* matrigel network formation assay

Endothelial cell network formation assays were performed using growth factor reduced (GFR) Matrigel (BD Bioscience, Cat. No. C354230) or standard growth factor Matrigel (BD Bioscience, Cat. No.356234). Briefly, each well of a 96-well plate was coated with 50ul of Matrigel and incubated at 37ºC for 30 min to promote polymerization. ECs were harvested and counted using Trypan Blue exclusion. Approximately 2 x 10^4 cells were seeded in each well with 200ul EGM-MV2+0.5% FBS media. TIFF images of capillary-like network were captured using a Nikon TE2000 inverted microscope and processed using the Angiogenesis ImageJ software.

2.18. Behavioral assays

Prior to the behavioral testing, all animals were left to acclimatize to an inverted light cycle housing room for 10 days and handled once a day for 1 week. Behavioral tests were completed at University of Ottawa's Behavior Core Facility between 9am and 5pm under dim red light. On testing day before the task, animals were habituated to the testing room for 60 minutes. Behavior tests were

performed with all mice in the following order: Novel Object Recognition (2 days), Rotarod (7 days), Beam Break (7 days), Social Interaction with Ultrasonic vocalization (1 day). The Marble Burying test (1 day) was performed with a different cohort of mice. All tests were directly inspired (or slightly modified) from published studies[144, 146, 147, 156-158].

Novel Object Recognition test (NORT). A 2-day NORT was as previously described[144]. On day one, 24hours before the actual experiment, each animal was habituated to an empty open field arena (45cm x 45cm x 45cm) for 30 min. On experimental day, mice were habituated for a second time to the open field for 10 min. Following habituation, each mouse was removed from the open field and placed in a clean holding cage for 2 min. Two identical objects (red cup or white funnel) were placed in the arena and the mouse is returned to the arena for a 10 min familiarization period. The mouse was removed from the arena and placed in a clean holding cage for 1 hour. After the mouse was left undisturbed for one hour, the object recognition test consisted in one cleaned familiar object and one cleaned novel object (red cup or white funnel switched). The mouse was returned to the arena for a 5 min recognition period. All interactions with the objects were recorded using Ethovision 7 XT software (Noldus). Object recognition was scored as the time during which the nose of the animal was located within 2 cm of the object. A discrimination index was calculated as: [time spent sniffing novel object/ (time spent sniffing novel object + time spent sniffing familiar object)].

Rotarod test. Motor coordination was assessed using a rotarod apparatus equipped with automatic timers as well as falling sensors, using the protocol from Cao *et al.* 2015[156]. Each mouse was placed on a textured rod (IITC Life Science) and left for 5 minutes to acclimatize prior to movement. The rod accelerates gradually from 4 to 40 rpm for 300seconds. When the mouse falls, the magnetic triggers record the rotational speed (rpm), duration (seconds) and distance traveled

(meters). The test was repeated for a period of 7 days with a total of 6 trials per day, with 15minutes inter-trial intervals (ITI).

Beam Break test. Locomotor activity was monitored using infrared beam break system as in [146]. Mice were individually housed in separate cages (27cm x 16cm x 13cm) with clean bedding. A maximum of 24 animals were tested at once. Each cage was placed in a metal frame and general motor activity was measured during 7 consecutive days for 24hrs per day using Micromax analyzer software (Omnitech Electronics). The first day was considered habituation and not included in locomotor activity average (Figure.21A). Horizontal activity counts (beam breaks) were recorded. At the end of the paradigm, mice were removed from testing cages and returned to their home cages.

***Social interaction test (SIT) with ultrasonic vocalizations (USV*).** A three-phase male-female SIT-USV was performed as in Yang *et al.* 2015[147]. Prior to testing, males *16p11.2*^{Vasc} subjects and stimulus *Cdh5-Cre*$^{tg/+}$ females were group-housed by sex, and sexually naïve. Females were visually inspected for estrus cycle, as previously described [157]. Only females in proestrus or estrus were used as stimulus mice. A control (*Cdh5-Cre*$^{tg/+}$) estrus female was placed in a small rectangular wire mesh enclosure at one side of an open field box (45cm x 45cm x 45cm). Interactions with the control female mouse were video recorded and monitored using Ethovision 7 XT software. The test consisted of three phases: Phase 1, the male interacts with an unfamiliar female for 5 min. Phase 2, the female is removed for 3 min, leaving the male alone in the arena. Phase 3, the same female is returned for 3 min. One female interacted with 2 males per testing day, with 30 minutes between each interaction. Time spent by the male in the rectangular interaction zone (2cm from female enclosure), as well as time spent in two open field corners away from female, were recorded. USVs were continuously recorded during the test by an ultrasonic

microphone (Ultravox XT by Noldus) mounted on the outside of the wire mesh female enclosure. As explained in [147], USVs are produced by the male in this context.

Marble Burying test. This test was performed as previously described in [158]. The test consisted in a 30 min trial per mouse. For each trial, a standard polycarbonate rat cage (26 cm x 48 cm x 20 cm) filled with 5 cm-thick SANI-chip bedding was used on which 20 marbles were evenly distributed (5 rows of 4 marbles). Each mouse was placed at the bottom left corner of the cage. During the test, the cage was covered by transparent Plexiglas. Once the trial was completed, the number of marbles that were either fully buried, or at least 2/3 covered by bedding, were counted as 'buried'.

2.19. Statistical analysis

All data analysis was conducted blindly to the genotype/experimental condition, and all statistical tests were performed using GraphPad Prism 8.0 Software. A Mann-Whitney U test (appropriate for small sample size - each animal being considered as a sample) was used for two group comparisons between WT and *16p11.2*$^{df/+}$ mice (and between *Cdh5-Cre*$^{tg/+}$ and *16p11.2*^{Vasc} mice) for metrics including CBF kinetics, vascular density and branching at a specific age, filopodia extension number, number/coverage of cellular types, mean capillary diameter, as well as cerebral cortex anatomical indices. A 2way ANOVA (e.g. 'genotype x age' or 'treatment x time') and a *post-hoc* test (Sidak's or Turkey's multicomparison), with repeated measure when appropriate, was used for vascular reactivity, endothelial network growth, and behavioral readouts. $P < 0.05$ was considered significant.

3. Results

3.1. Objective #1: *Examine the health of the brain vasculature in a genetically-engineered mouse model of the 16p11.2 deletion syndrome.*

Rationale. Reports on ASD patients demonstrated abnormal cerebral perfusion using ASL-fMRI and SPECT analysis [88]. These studies were able to correlate abnormal cortical perfusion rates with symptom severity [61]. In addition, 16p11.2 deletion carriers display abnormal brain structure [71, 143]. Here, in order to clarify the link between ASD and the brain vasculature, we investigated cerebrovascular function, structure and integrity in *16p11.2*$^{df/+}$ mice and WT littermates at postnatal day 14 (P14, peak in cerebral cortex vascular density) [24] and P50 (when angiogenesis stabilizes and NVC is functional) [5].

3.1.1. Behavioral assessment of adult *16p11.2*$^{df/+}$ mice

In the first part of this study, constitutive *16p11.2*$^{df/+}$ mutants and their WT littermates underwent behavioral testing to evaluate our ability to reproduce published ASD-related behaviors.

When compared to WT littermates, *16p11.2*$^{df/+}$ mice revealed increased home cage activity during their active (night) phase in a 7-day beam break test (Figure 3A, page 37), as published by the group of Dr. Ted Abel [146]. However, in our hands males and females displayed phenotypic differences, as only *16p11.2*$^{df/+}$ males demonstrated a significant increase in activity during the dark phase. Already from the habituation period (first 12 hours of the test), *16p11.2*$^{df/+}$ males were more active than WT littermates, whereas *16p11.2*$^{df/+}$ females did not reveal differences during the same period (Figure 3A, page 37). In addition, *16p11.2*$^{df/+}$ mice displayed significant motor coordination differences following a long-term (7 days) rotarod test. While the overall group of mutants performed better than WT controls, this difference was due to males but not females

(Figure 3C, *top panels,* page 37). Separate trials demonstrated a significant difference between *16p11.2*$^{df/+}$ and WT littermates at trial 37 and 41 where *16p11.2*$^{df/+}$ males and females (Figure 3C, *bottom panels,* page 37). More animals will be added to complete the group of females in the rotarod test. Finally, *16p11.2*$^{df/+}$ mice do not show significant differences in the marble burying test (Figure 3E, page 37). Of note, none of those two tests (rotarod and marble burying) were previously published using *16p11.2*$^{df/+}$ mice.

Moreover, as recently published[144], the NORT revealed that *16p11.2*$^{df/+}$ males do not show preference for the novel object, and interacted for a longer period of time with the familiar object, when compared to WT littermates (Figure 3G, page 37). These results comfort us in the use of these tests in Objective 3.

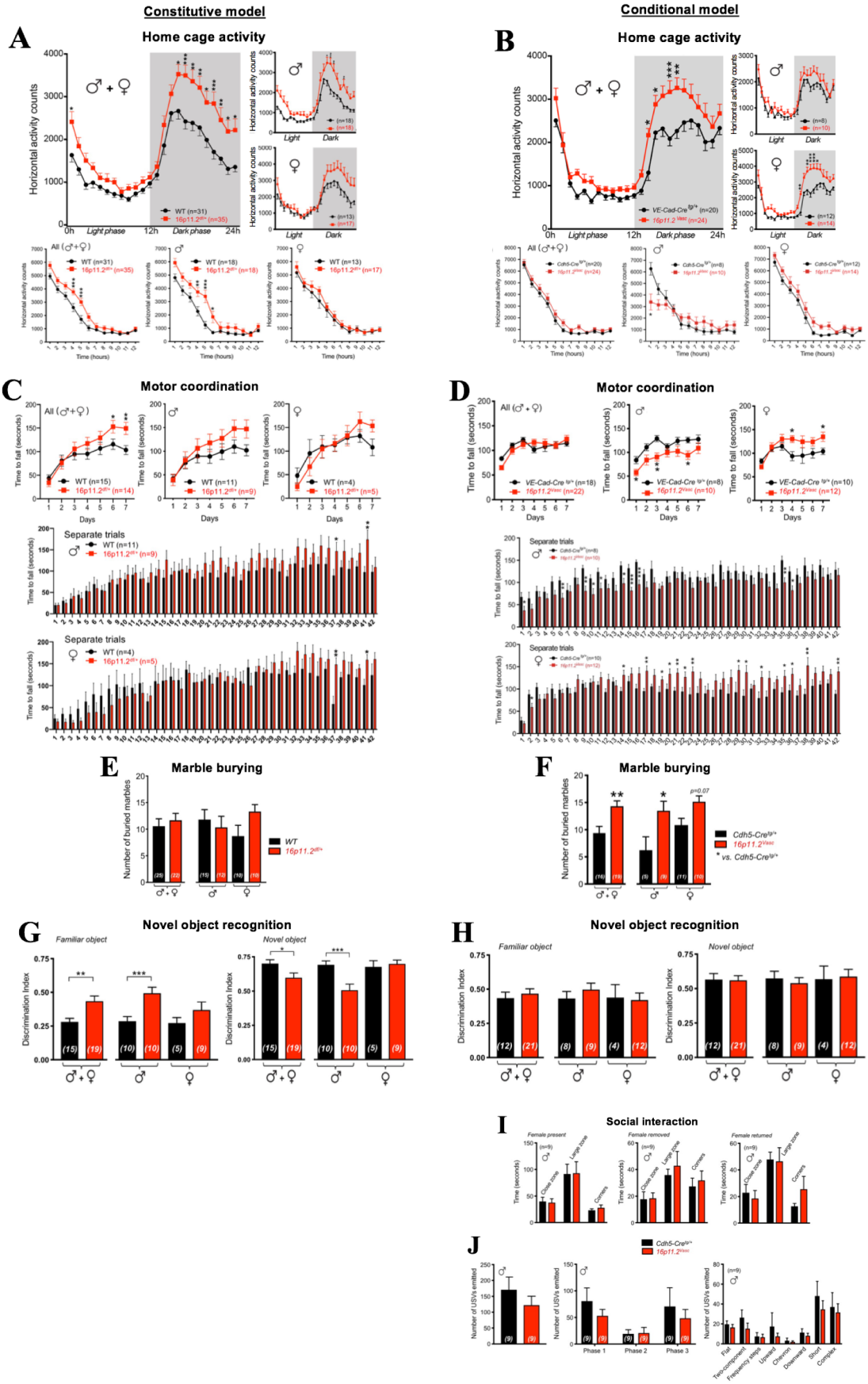
Constitutive model
Conditional model
A
Home cage activity
B
Home cage activity
C
Motor coordination
D
Motor coordination
E
Marble burying
F
Marble burying
G
Novel object recognition
H
Novel object recognition
I
Social interaction
J

Figure 3 (page 37)**. ASD-related behaviors in *16p11.2$^{df/+}$ (left)* and *16p11.2^{Vasc} (right)* mice.** **(A-B)** *Top panels*, Home cage hyperactivity identified in *16p11.2$^{df/+}$* **(A)** and *16p11.2^{Vasc}* **(B)** males and females. *Bottom panels*, First 12hrs of habituation (testing day 1 of 7) from beam break test. Male *16p11.2$^{df/+}$* mutants displayed increased activity between hour 4 and 6 of the habituation period while male *16p11.2^{Vasc}* mutants displayed a slight habituation deficit during the 3 first hours. **(C-D)** *Top panels,* Motor coordination abnormalities measured over 7 days using rotarod. *Middle and bottom panels*, Separate rotarod trials across the entire duration of the test (7 days, 6 trials per day, total of 42 trials). **(E)** Marble burying in *16p11.2$^{df/+}$* mice compared to control littermates, in a sex-dependent manner. **(F)** Increased marble burying in *16p11.2^{Vasc}* mice compared to control littermates, in a sex-dependent manner. **(G-H)** Two-day novel object recognition test in *16p11.2$^{df/+}$* compared to WT littermates **(G)** and *16p11.2^{Vasc}* compared to control *(Cdh5-Cre$^{tg/+}$)* mice **(H)**. Discrimination index of the difference in exploration time between familiar object (*left panel*) and novel object (*right panel).* **(I)** The social interaction test with ultrasonic vocalizations failed to reveal differences between *16p11.2^{Vasc}* and control mice (males). **(J)** *Left panel,* Bar graphs represent overall USVs. *Middle panel,* Number of USVs during each phase of the test. *Right panel*, Illustrate different categories of USVs based on their phonological signature. All data are mean ± s.e.m. (n=4-18 animals per group; n=10-35 animals per genotype). *$P < 0.05$, **$P < 0.01$, ***$P < 0.001$ (2way ANOVA and Sidak's *post-hoc* test for sex differences; 2way repeated measure ANOVA and Sidak's *post-hoc* test).

3.1.2. Assessing cerebrovascular function in *16p11.2*$^{df/+}$ mice

In this part of the study, functional assessments were performed on anesthetized *16p11.2*$^{df/+}$ mice to determine if this model demonstrates CBF and/or brain metabolism deficits. Cerebral blood flow was measured in the two age groups, P14 and P50, both critical time points in postnatal vascular development. The cerebral cortex (subdivided in anterior, parietal, and occipital regions) represented the focus of these functional assays.

Non-invasive ultrasound imaging of intravenously-injected microbubbles revealed elevated resting-state perfusion in the parietal cortex of *16p11.2*$^{df/+}$ males (Figure 4, page 41). Region of interest area (representative of blood volume) was not different between *16p11.2*$^{df/+}$ and WT littermates, while peak enhancement, wash-in rate and wash-in perfusion index (representative blood flow) appeared elevated in P50 *16p11.2*$^{df/+}$ mice (only tested males in this case). Time to reach maximum perfusion was not altered between WT and mutant males (Figure 4, page 41), but baseline was maintained higher.

We then assessed activity-dependent regulation of CBF using laser Doppler flowmetry (LDF) over the primary somatosensory cortex. At P14, NVC responses to whisker stimulation in *16p11.2*$^{df/+}$ and WT mice showed no difference. However, hemodynamic responses appeared significantly reduced and slower in P50 mutant mice (Figure 5A, page 42). In adult *16p11.2*$^{df/+}$ males, we identified an elevated resting-state CBF, a reduced CBF increase from baseline, as well as an increased time to return to baseline (Figure 5A, page 42). Although adult *16p11.2*$^{df/+}$ mice displayed elevated baseline CBF during both ultrasound contrast imaging and LDF, this phenotype was not attributed to cardiovascular dysfunction, since systolic blood pressure and heart rate were not altered (Figure 5B, page 42), suggesting the existence of a central mechanism. Furthermore, similar CBF analysis were completed in P14 and P50 *16p11.2*$^{df/+}$ female mice that did not display

overall alteration in CBF when compared to sex-matched WTs. However, LDF revealed slower kinetics in P14 *16p11.2*$^{df/+}$ females, as depicted by attenuated falling slope (Figure 6A, page 43). Interestingly, CBF differences were also identified between male and female mice (Figure 6B, page 43). In particular, P50 WT and *16p11.2*$^{df/+}$ female mice showed reduced resting-baseline values and elevated response amplitudes when compared with P50 *16p11.2*$^{df/+}$ males. All other parameters analyzed were not different between males and females.

Next, we measure resting-state glucose uptake in adult male *16p11.2*$^{df/+}$ and WT mice using [^{18}F]-2-fluorodeoxyglucose positron emission tomography (FDG-PET scan). This assay revealed a significant overall increase in glucose uptake in adult male and female *16p11.2*$^{df/+}$ mice compared to age-matched WT littermates (Figure 7A, page 44). In addition, no difference in oxygen delivery, extraction and total hemoglobin were identified between male *16p11.2*$^{df/+}$ and WT mice while measuring brain blood oxygen saturation (sO_2) using photoacoustic imaging (Figure 7C-D, page 44).

To test brain vessel function, we assessed vascular reactivity (VR) of the middle cerebral artery (CNS) and mesenteric artery (periphery). This experiment allowed us to measure endothelium-dependent and VSMC-dependent control of vascular tone (Figure 8A, page 45). The contribution of brain EC and/or VSMCs to 16p11.2 deletion-associated CBF alterations were assessed by measuring diameter changes of pressurized middle cerebral arteries (MCA) to increasing vasomodulator concentration *ex vivo* (Figure 8B, page 45). Endothelial-specific deficits in *16p11.2*$^{df/+}$ MCAs were evidenced by i) reduced vessel relaxation in response to acetylcholine (Ach), ii) impaired vasoconstriction following endothelial nitric oxide synthase (eNOS) inhibition, and iii) reduced relaxation by adenosine, in both males and females (Figure 8B-C, page 45). Furthermore, we demonstrated intact VSMC response to phenylephrine (PE), and to exogenous

NO using NO donor SNP (Figure 8B-C, page 45). Additionally, a similar endothelium-dependent VR deficit was measured *ex vivo* in mesenteric arteries (Figure 8D, page 45). Altogether, these findings demonstrate a close correlation between global CBF dysregulation and endothelial-specific impairments in *16p11.2*$^{df/+}$ mice.

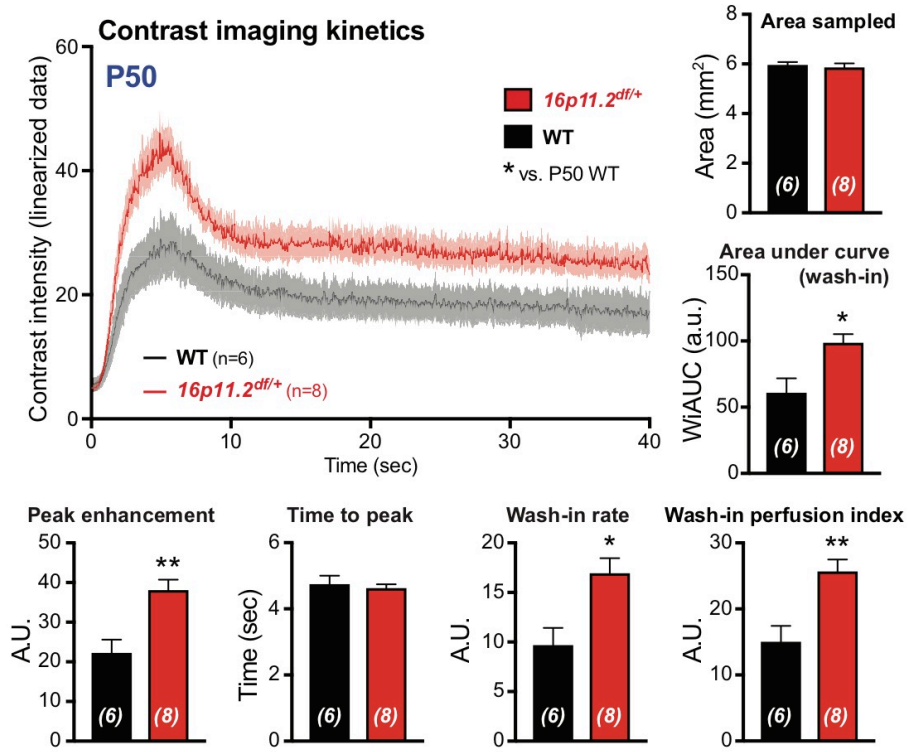

Figure 4. Resting-state perfusion in the somatosensory cortex of *16p11.2*$^{df/+}$ males.
Ultrasound contrast imaging of i.v.-injected microbubbles in anesthetized mice at P50. Top left traces illustrate time/intensity values over a 40 second wash-in/wash-out period in somatosensory cortex. Bar graphs dissect parameters of microbubble resonance kinetics. Quantifications demonstrate a higher baseline CBF in 16p11.2$^{df/+}$ mice compare to WT controls. WT, wild type. All data are mean± s.e.m. (n=6-8 animals per group). *P < 0.05, ** P < 0.01 (Mann-Whitney test).

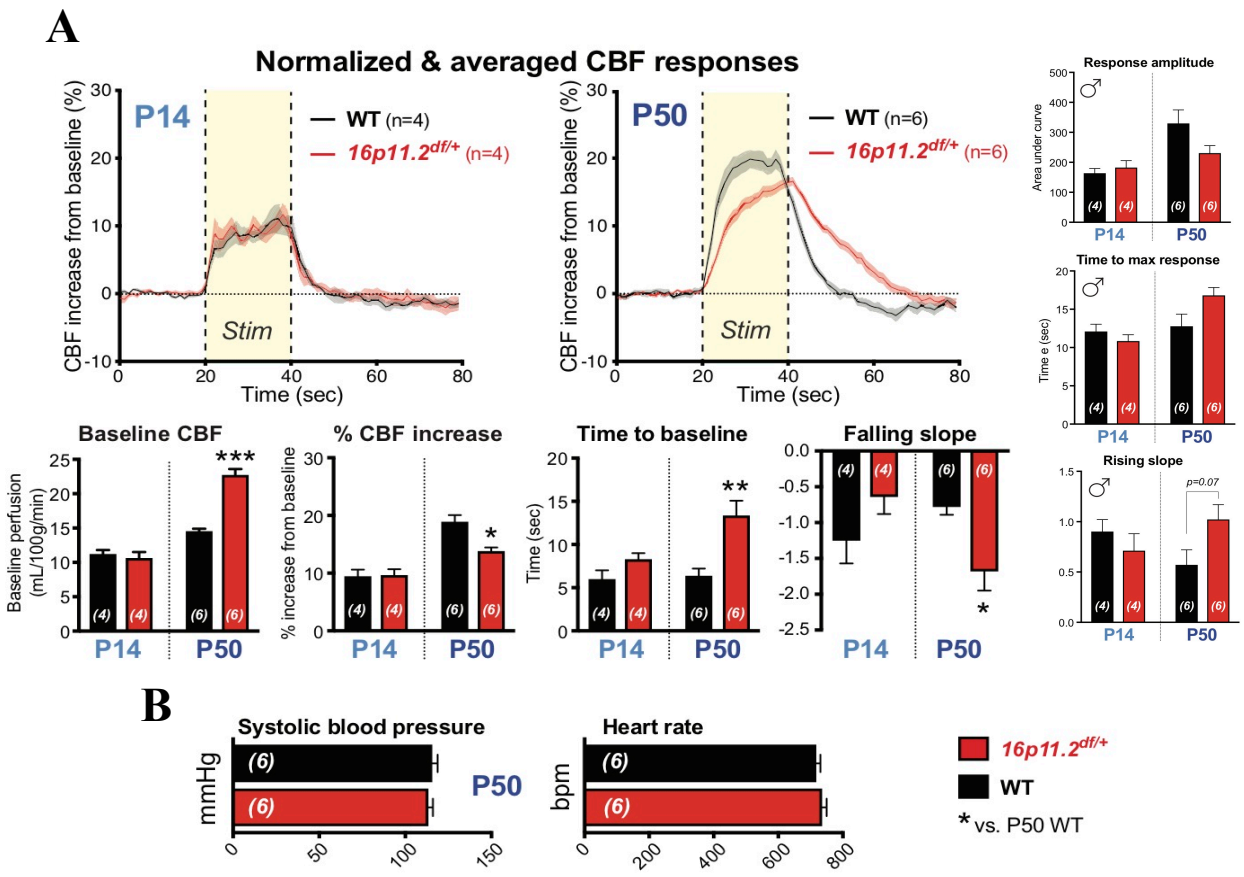

Figure 5. Activity-dependent regulation of cerebral blood flow (CBF) and systolic blood pressure in *16p11.2*$^{df/+}$ males.

(A) Laser Doppler flowmetry (LDF) coupled with whisker stimulation in anesthetized P14 and P50 male mice. Bar graphs represent hemodynamics parameters of CBF responses monitored over the primary somatosensory cortex. Adult 16p11.2df/+ mice demonstrate a neurovascular coupling defect. **(B)** Mean systolic blood pressure and heart rate measured over 5 days at P50 using tail cuffs. WT, wild type. All data are the mean ± s.e.m (n=4-6 animals per group). *P < 0.05, **P < 0.01, ***P < 0.001 (Mann-Whitney test).

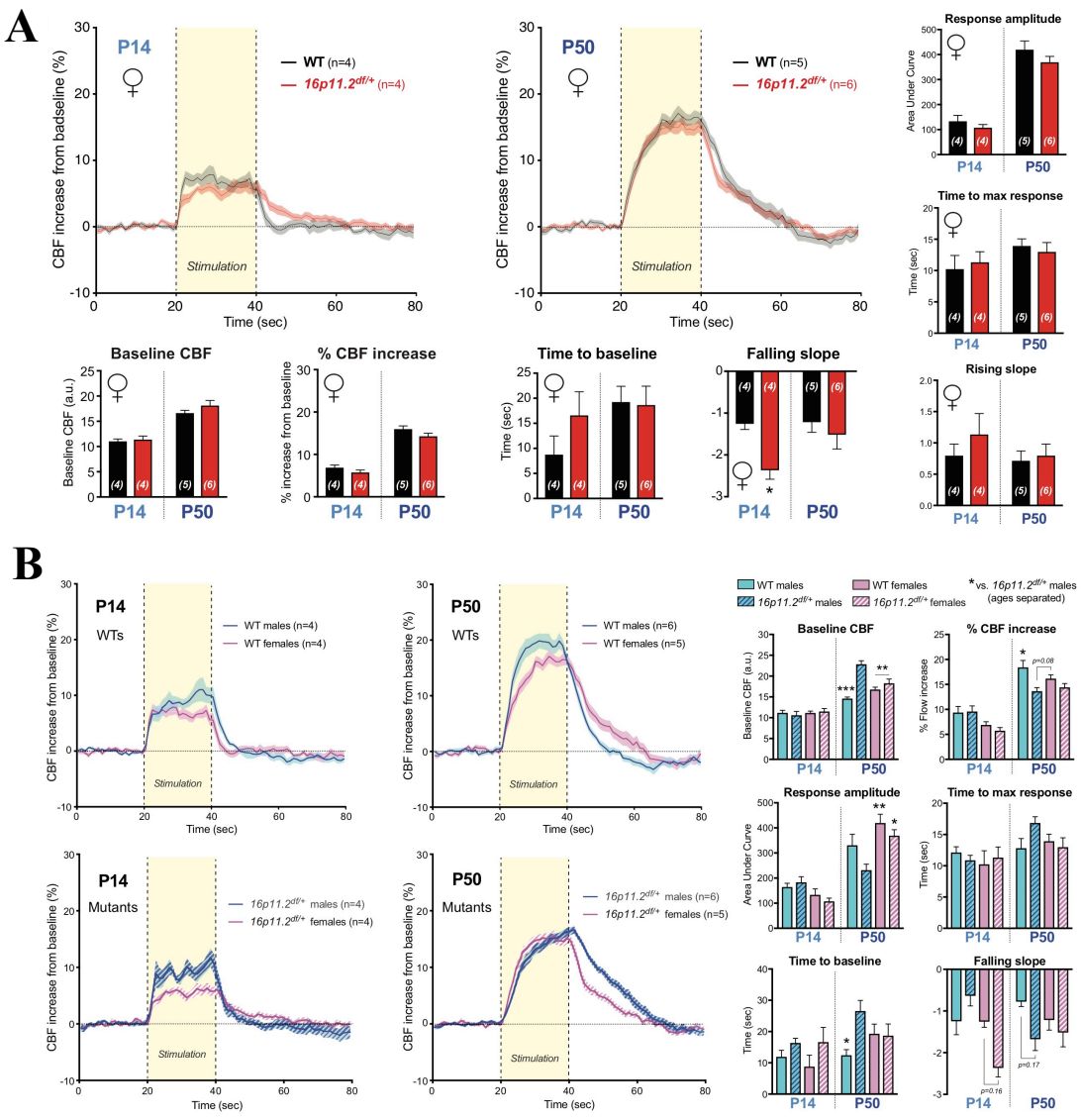

Figure 6. Cerebral blood flow measurements in *16p11.2*$^{df/+}$ and WT female mice.
(A) Laser Doppler flowmetry (LDF) coupled with whisker stimulation in anesthetized P14 and P50 female mice. Bar graphs represent hemodynamics parameters of CBF responses monitored over the primary somatosensory cortex. Only falling slope appeared significantly affected by genotype. **(B)** Comparison of CBF parameters between male and female mutant and WT mice. WT, wild type. All data are mean ± s.e.m (n=4-6 animals per group). $*P < 0.05$, $**P < 0.01$, $***P < 0.001$ (Mann-Whitney test in A; 2way ANOVA and Turkey's post-hoc test in B).

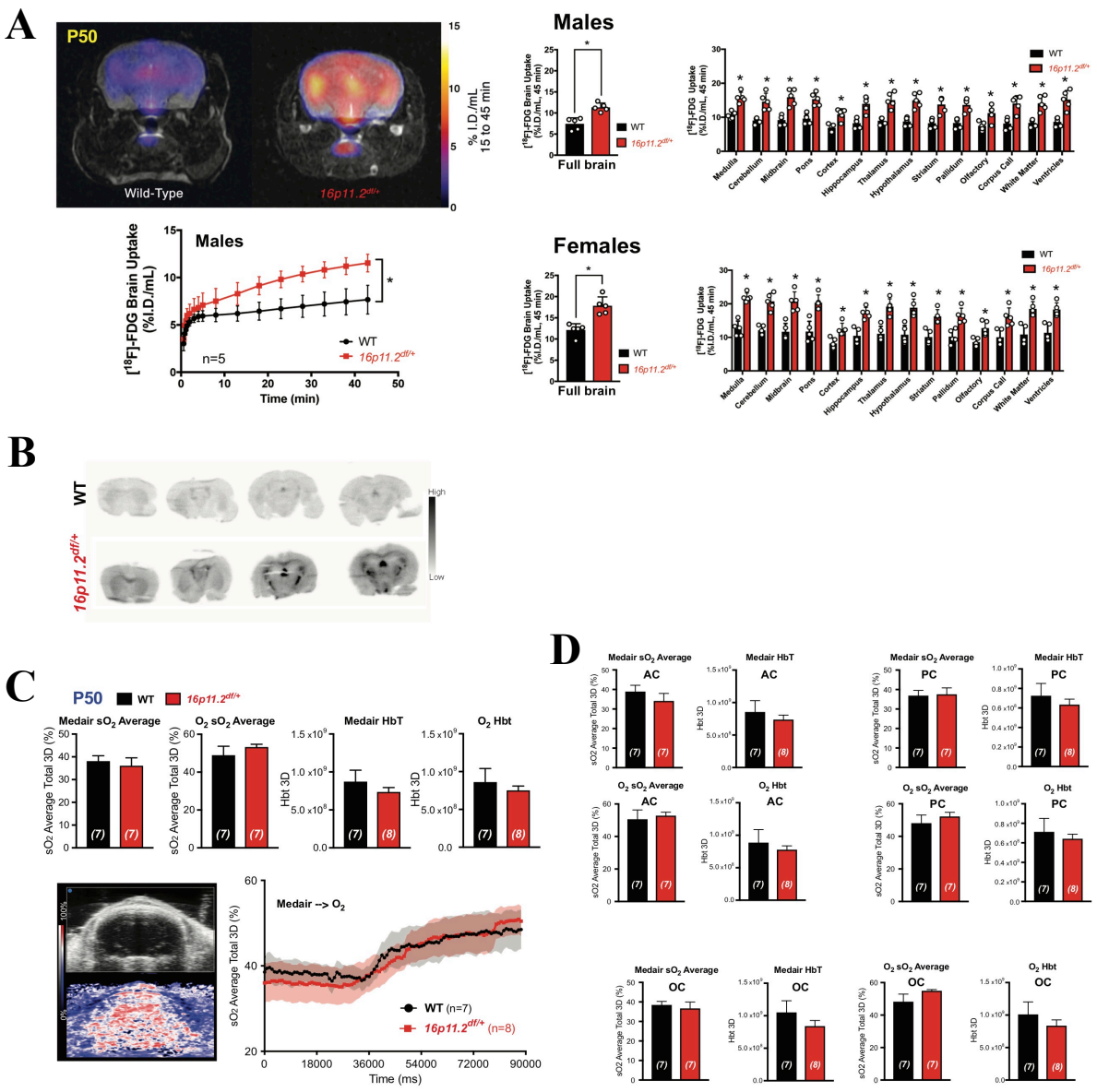

Figure 7. Brain metabolism in *16p11.2*$^{df/+}$ and WT P50 mice.

(A) Brain glucose uptake assessed by FDG-PET scan in isoflurane-anesthetized mice. Overall increase in glucose uptake was demonstrated in both males and females. **(B)** Autoradiographs showing increased FDG uptake is not due to increased perfusion, but to retention of FDG by brain cells. **(C)** Brain blood oxygen saturation (sO2) in ketamine/xylazine-anesthetized mice measured by photoacoustic imaging (PAI). *Bottom left*, ultrasound image and representative example of sO2 acquisition by PAI. Bottom right panel demonstrate oxygen delivery trace acquired by PAI during transition from regular air (Medair) to pure oxygen (O2) in the anesthesia mask. **(D)** Oxygen saturation measured by PAI in three major subdivision of the cerebral cortex. AC, anterior cortex; PC, parietal cortex; OC, occipital cortex; Hbt, total hemoglobin; WT, wild type. All data are mean ± s.e.m. (n=4-8 animals per group). **P* < 0.05 (Mann-Whitney test in bar graphs; 2way repeated measure ANOVA and Siddak's *post-hoc* test for trace).

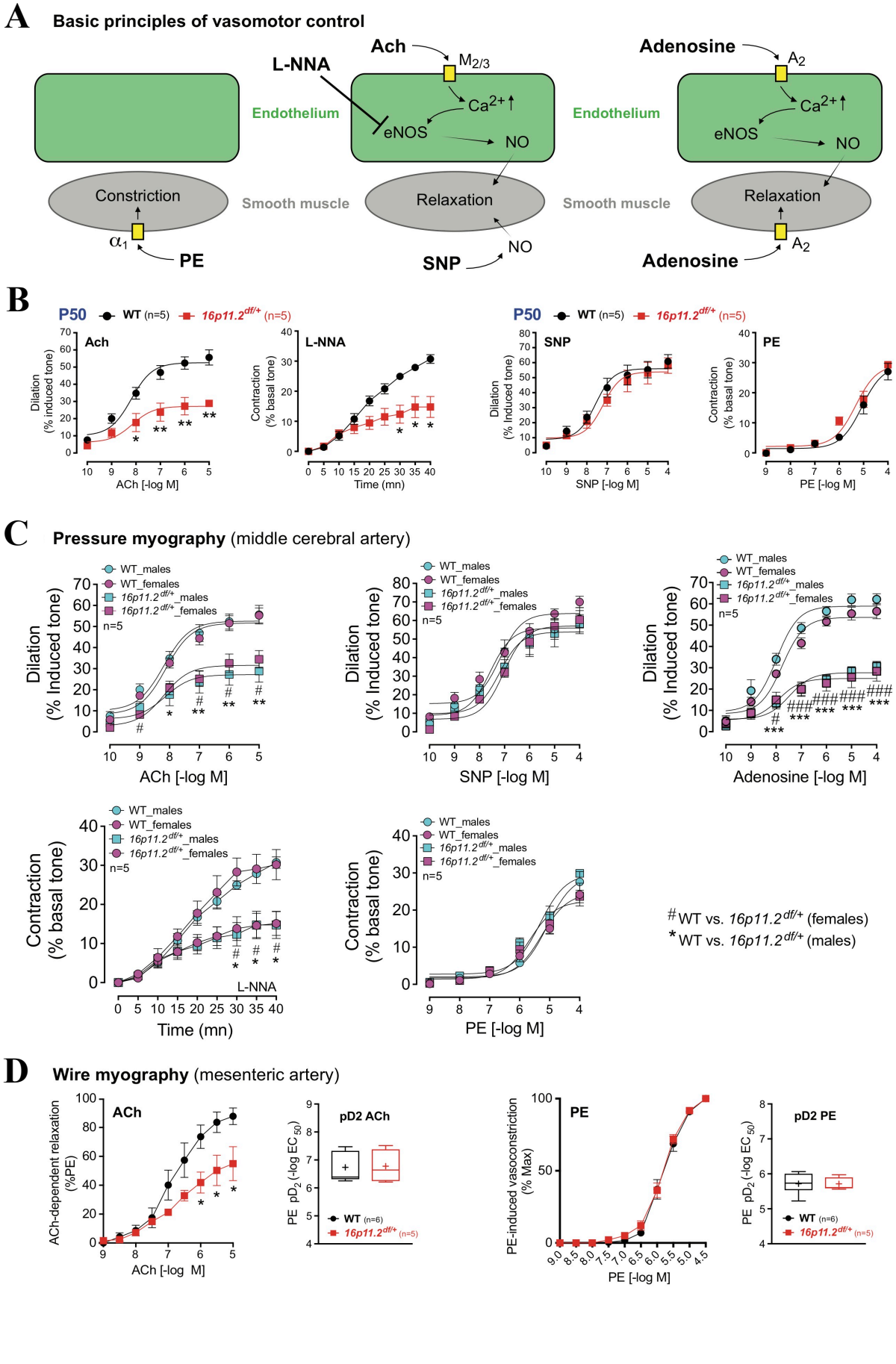
A
Basic principles of vasomotor control
Ach
M2/3
L-NNA
Endothelium
Ca2+
eNOS
NO
Adenosine
A2
Constriction
Smooth muscle
Relaxation
α1
PE
SNP
B
P50
WT (n=5)
16p11.2df/+ (n=5)
Ach
L-NNA
SNP
PE
Dilation (% induced tone)
Contraction (% basal tone)
Dilation (% Induced tone)
ACh [-log M]
Time (mn)
SNP [-log M]
PE [-log M]
C
Pressure myography (middle cerebral artery)
WT_males
WT_females
16p11.2df/+_males
16p11.2df/+_females
n=5
Adenosine [-log M]
L-NNA
#WT vs. 16p11.2df/+ (females)
*WT vs. 16p11.2df/+ (males)
D
Wire myography (mesenteric artery)
ACh-dependent relaxation (%PE)
pD2 ACh
PE pD2 (-log EC50)
PE-induced vasoconstriction (% Max)
pD2 PE

Figure 8 (page 45)**. Vascular reactivity of middle cerebral arteries and mesenteric arteries ex vivo in *16p11.2*$^{df/+}$ and WT mice at P50.**
(A) Schematic representation of cellular and molecular vascular reactivity mechanisms. **(B)** Pressurized middle cerebral arteries *ex vivo* reveals endothelium-dependent vasodilation but normal smooth muscle dependent vasoconstriction in *16p11.2df/+* males at P50. **(C)** Comparison of vascular reactivity of pressurized middle cerebral arteries between male and female mutant and WT mice. **(D)** *Ex vivo* wire myography on mesenteric arteries demonstrate endothelium-dependent deficits and normal smooth muscle cell responses. Ach, acetylcholine; L-NNA, NG-Nitro-L- arginine; PE, phenylephrine; SNP, sodium nitroprusside; WT, wild type. All data are mean ± s.e.m. (n=5-6 animals per group). *$P < 0.05$, **$P < 0.01$, ***$P < 0.001$ (Mann-Whitney test in B & D; 2way repeated measure ANOVA and Turkey's *post-hoc* test in C).

3.1.3. Assessment of brain vascular structure in *16p11.2*$^{df/+}$ mice

Notably, early after birth, the brain microvasculature undergoes rapid hypoxia-, genetic-, and activity-dependent maturation up to P14, where vascular density is at its highest in the cortex. Past P14 the neurovascular networks undergo remodeling/maturation until adulthood. Therefore, altered endothelial growth might affect CBF regulation.

To assess whether *16p11.2*$^{df/+}$ mice display altered endothelial growth, vascular network structure was analyzed at P14 and P50. The structure of CD31-positive endothelial networks of *16p11.2*$^{df/+}$ and WT mice was quantified in three major subdivisions of the cerebral cortex (anterior, parietal and occipital cortex) by computational reconstruction of endothelial networks using our validated integrative method (Figure 9A, page 47)[24]. At P14, endothelial network density and branching was significantly lower throughout the cerebral cortex in male *16p11.2*$^{df/+}$ mice compared to WT littermates (Figure 9B, page 47). At P50, endothelial network structure was similar between *16p11.2*$^{df/+}$ and WT male mice, with the exception of the parietal cortex layer IV where mutant mice demonstrated elevated vascular branching and density (Figure 9B, page 47). This effect was only found in males, since *16p11.2*$^{df/+}$ and WT female littermates displayed similar patterns throughout the three regions of cortex as well as in different cortical layers (Figure 10, page 48). The endothelial specificity of this *16p11.2*$^{df/+}$-associated structural phenotype was

supported by normal assembly of NVU cells around the endothelium (Figure 11, page 49). Indeed, normal development of pericytes (Figure 11A, page 49), VSMCs (Figure 11B, page 49), astrocytes (Figure 11C, page 49), and microglia (Figure 11D, page 49) was found in P14 and P50 *16p11.2*$^{df/+}$ mice when compared to WTs.

Therefore, the postnatal *16p11.2*$^{df/+}$ cerebral cortex is characterized by delayed endothelial network growth.

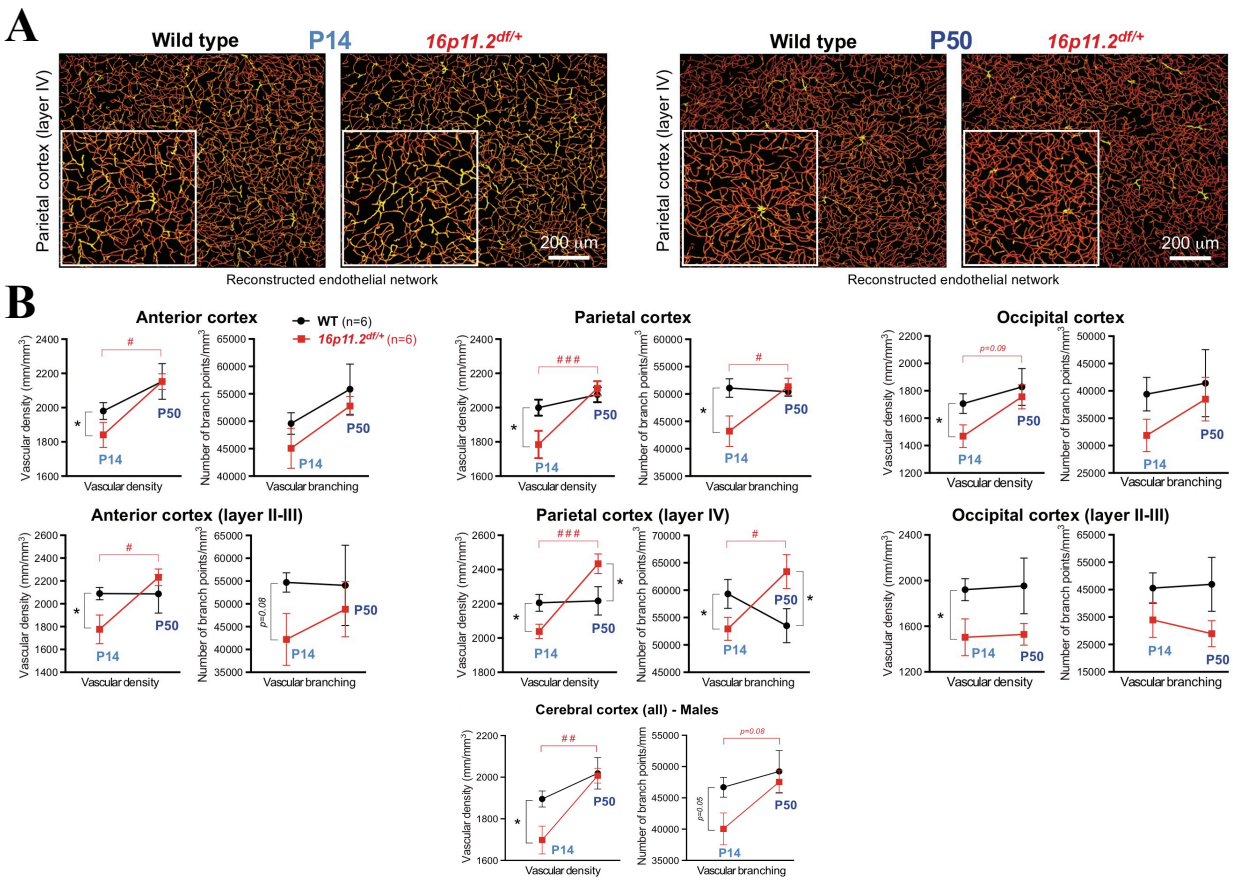

Figure 9. Cortical endothelial network structure of *16p11.2*$^{df/+}$ males.
(A) Z-projection images of 3D vascular network reconstruction examples (CD31-stained endothelium), illustrating lower vascular density at P14, and a higher density at P50 in primary somatosensory cortex of *16p11.2*$^{df/+}$ mice. **(B)** Quantifications (computational image analysis) of endothelial network in three major subdivisions of the cerebral cortex and cortical layers at P14 and P50. Widespread endothelial network delay at P14 in *16p11.2*$^{df/+}$ male mice. WT, wild type. All data are mean ± s.e.m. (n=3-8 animals per group). **P* < 0.05 (Mann-Whitney test). #*P* < 0.05, ###*P* < 0.001 (2way ANOVA and Sidak's *post-hoc* test).

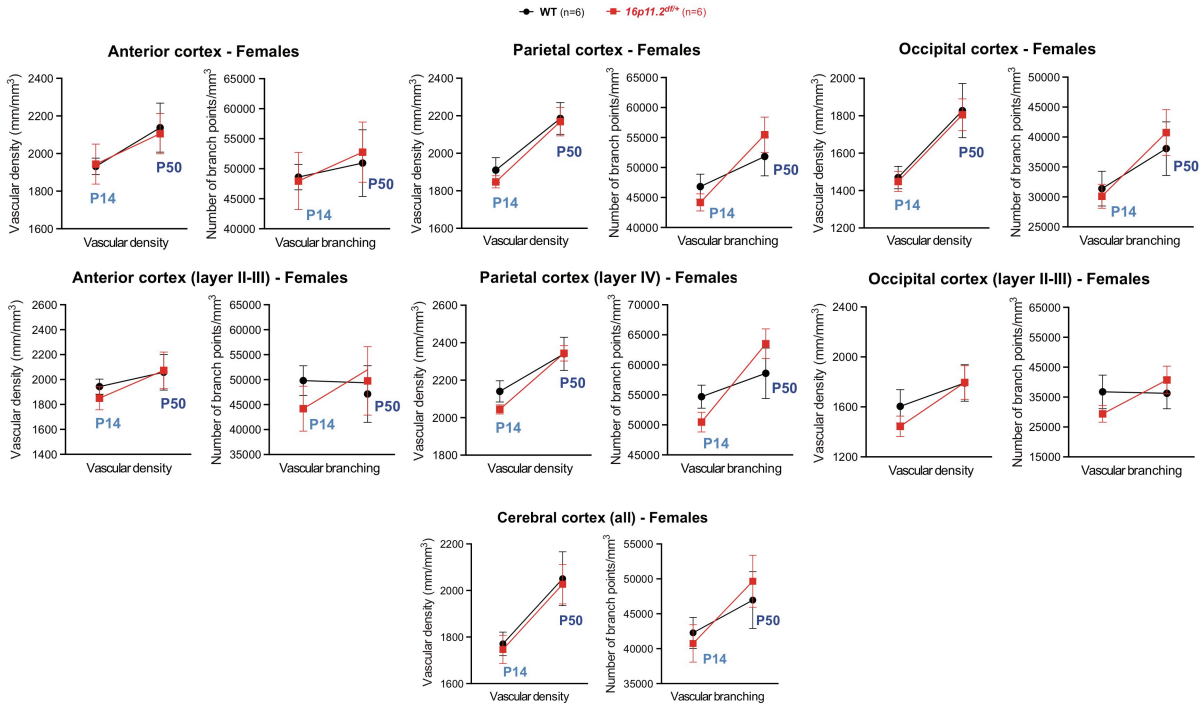

Figure 10. Postnatal developmental profile of the whole cerebral cortex endothelial networks in *16p11.2*$^{df/+}$ and WT females.

Quantifications of postnatal developmental profile of endothelial networks in subdivisions of the cerebral cortex and cortical layers. WT, wild type. All data are mean ± s.e.m. (n=6 animals per group; 2way ANOVA and Sidak's *post-hoc* test).

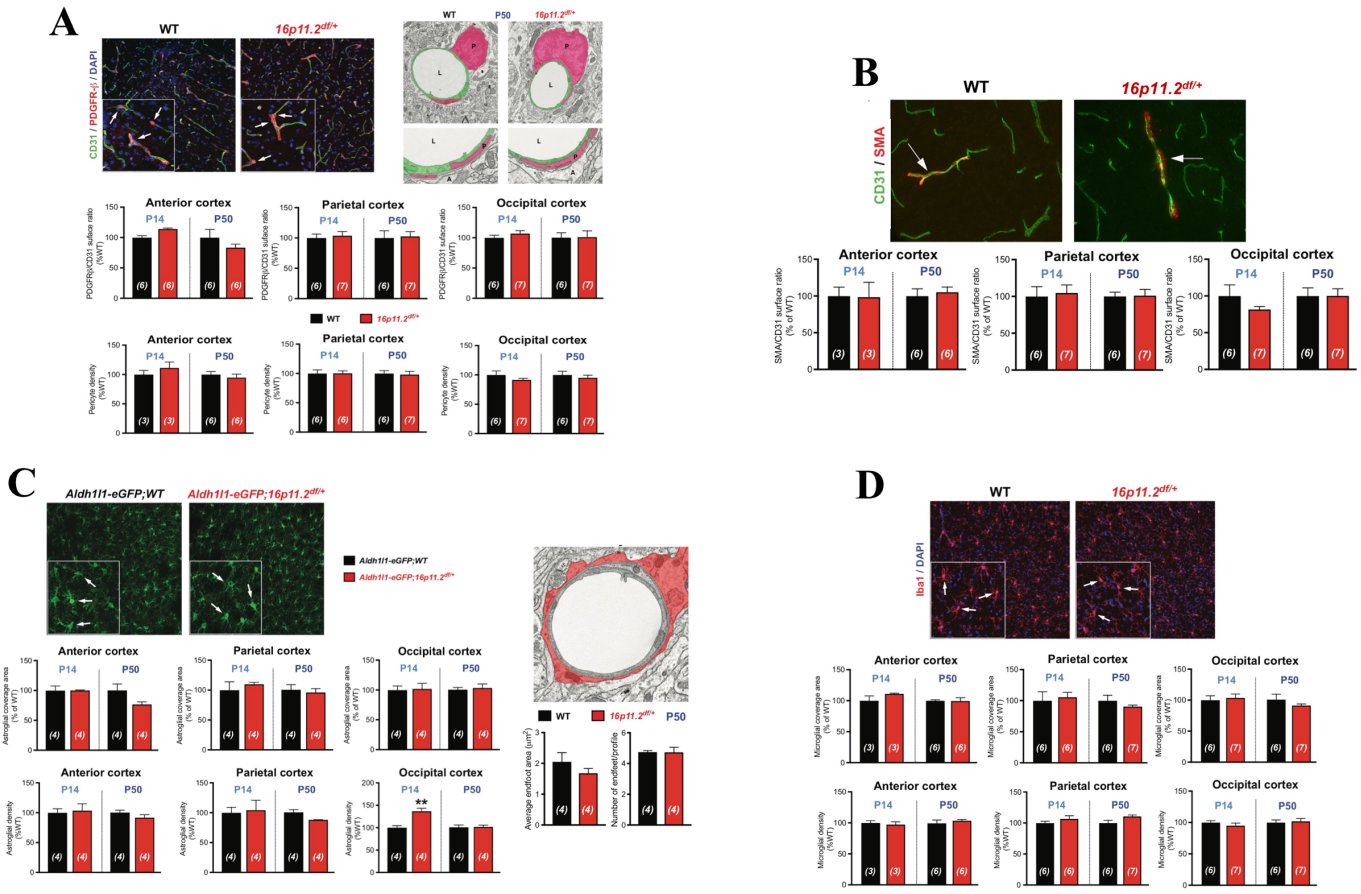

Figure 11. Development of neurovascular unit at P14 and P50 in *16p11.2*$^{df/+}$ and WT mice.
(A) *Left*, Immunohistochemical images of pericytes (PDGFR-b). *Right,* Transmission electron microscopic analysis of pericyte (pink) ultrastructure around brain capillaries (green). *Bottom panels,* Analysis of pericyte density and surface ratio measured in the anterior, parietal and occipital cortex. Normal pericyte attachment is observed in *16p11.2df/+* mice. (**B**) *Top images*, Immunohistochemical images of smooth muscle cells. *Bottom panels*, quantifications of of SMA/CD31 surface ratio in the anterior, parietal and occipital cortex. **(C)** Analysis of astrocyte density and surface coverage between *Aldh1l1-eGFP;16p11.2df/+* and control (*Aldh1l1-eGFP; WT*) mice. No differences were identified except for increased cell density in the occipital cortex at P14. **(D)** Analysis of microglial density and surface coverage between *16p11.2df/+* and WT littermates. No differences between genotype were observed. L, lumen; P, pericyte; WT, wild type. All data are mean ± s.e.m. (n=3-7 animals per group). $^{**}P < 0.01$ (Mann-Whitney test).

3.2. Objective #2: *Determine the cellular and molecular mechanisms underlying ASD- associated brain endothelial deficits.*

Rationale. The identified functional and structural differences in the *16p11.2*$^{df/+}$ mice demonstrate endothelial defects. Endothelial cells are the building blocks of blood vessels and are also directly involved in vasodynamic responses. In addition, genes in the 16p11.2 locus are related to the regulation of cellular proliferation, differentiation, morphology and motility, processes that play fundamental roles in developmental angiogenesis. By directly investigating endothelial cells, we can investigate consequence(s) of 16p11.2 haploinsufficiency on their function in a cell autonomous manner.

3.2.1. Phenotypes of murine endothelial cells carrying the 16p11.2 deletion

Brain endothelial network expansion and remodeling are regulated at the cellular and molecular level. Both of these processes consist of endothelial cell differentiation, proliferation and tubularization. To assess cellular phenotypes, P14 *16p11.2*$^{df/+}$ and WT male primary cerebral cortex endothelial cells (cECs) were isolated. Endothelial cell identity was confirmed using immunocytochemistry with endothelial-specific markers (VE-Cadherin and CD31) and qPCR using mouse VEGFR2, CD31 and eNOS (Figure 12A-B, page 51).

An *in vitro* matrigel-based network formation assay (MNFA) revealed that *16p11.2*$^{df/+}$ cECs display impaired network forming/remodeling ability compared to WT cECs (Figure 13A, page 52). VEGF supplementation of the matrigel failed to rescue this phenotype, confirming an intrinsic endothelial defect (Figure 13A, page 52). Furthermore, to determine whether *16p11.2*$^{df/+}$ cECs were in a more proliferative state, which could explain the MNFA phenotype, cell cycle analysis was completed using *16p11.2*$^{df/+}$ and WT cECs. No difference between *16p11.2*$^{df/+}$ and WT cECs in proliferative state was evidenced (Figure 13B, page 52). These results demonstrate

that 16p11.2 haploinsufficiency leads to cell-autonomous endothelial deficits in angiogenesis, revealing a novel aspect of the 16p11.2 deletion syndrome at the cellular level.

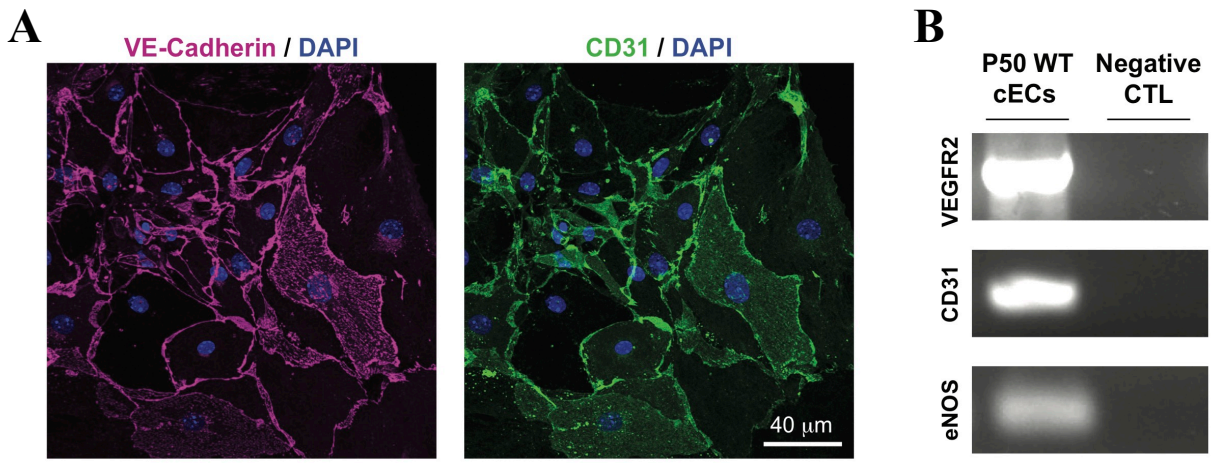

Figure 12. Characterization of primary male mouse cerebral cortex endothelial cells (cECs).
(A) Immunocytochemical identification of cultured cECs with endothelial-specific markers VE-Cadherin and CD31. **(B)** qPCR validation on cEC RNA using mouse VEGFR2, CD31 and eNOS as markers (HUVEC RNA used as negative control).

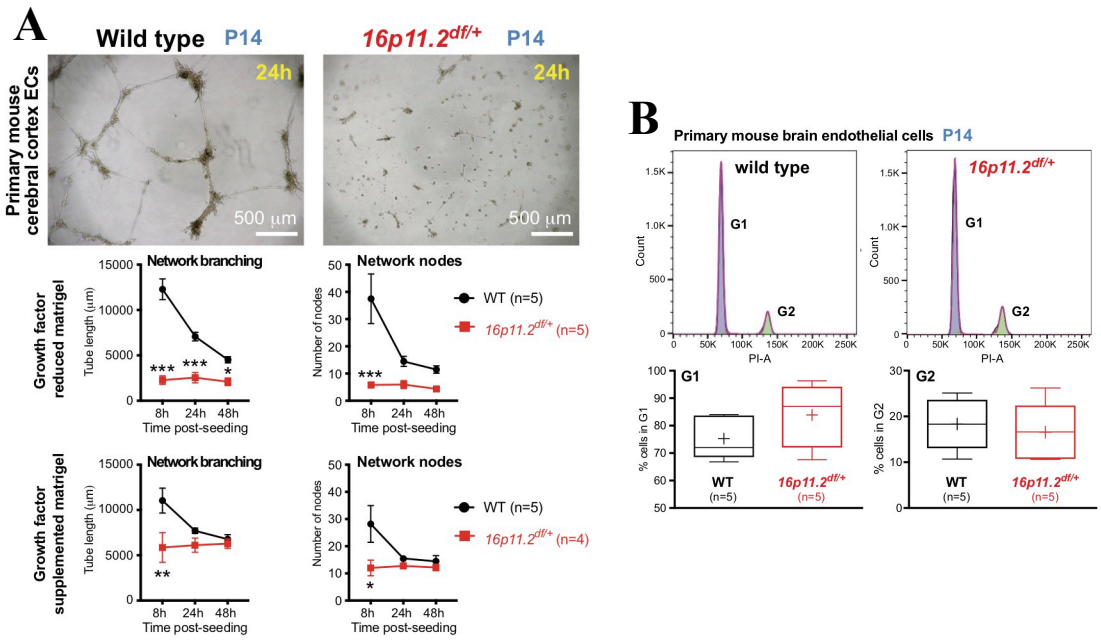

Figure 13. Assessment of cortical endothelial cells network formation ability and proliferation.

(A) *In vitro* matrigel- based network formation assay using P14 primary cerebral cortex endothelial cells (cECs) over a 48h period, to assess vascular network remodeling in a growth factor-reduced or -supplemented environment. Defective network formation in *16p11.2*$^{df/+}$ ECs compared to WT cells. *Top panels*, representative images at 24h time point. *Bottom panels*, quantification of network branching (endothelial tube length) and network nodes (node number). **(B)** Assessment of cEC proliferation using cell cycle analysis. Quantification of cECs in G2 (proliferation) versus G1 (growth) phase on cells isolated from P15 males. All data are mean ± s.e.m.

3.3. Objective #3: *Investigate the endothelial contribution to ASD-related phenotypes using a conditional, cell-specific genetic approach.*

Rationale. The integrity of the brain vasculature is critical for the establishment and function of neural circuits during development [2]. Defects in the brain vasculature has been linked to neurodevelopmental disorders such as cerebral palsy [159]. As both nervous and vascular systems highly depend on each other to coordinate their actions, we can therefore contemplate the idea that endothelial-specific 16p11.2 haploinsufficiency will trigger defects in cerebrovascular development, in turn affecting brain maturation and function.

3.3.1. Characterization of endothelial-specific 16p11.2 haploinsufficiency in vivo

Normal vascular development is required to ensure proper establishment of neural circuits, however, the impact of endothelial 16p11.2 haploinsufficiency on brain maturation is unknown. To assess the implication of cell-autonomous endothelial defects to 16p11.2 deletion-associated phenotypes, mice were generated for an endothelium-specific 7qF3 haploinsufficiency (*Cdh5- Cre*$^{tg/+}$*;16p11.2*$^{flox/+}$, that we named '*16p11.2*^{Vasc}'; see Figure 14A, page 55).

Following endothelial network structure analysis at birth (P0), the endothelial-specific 16p11.2 hemizygosity resulted in a mosaic expression pattern, allowing comparison of WT and haploinsufficient cECs *in vivo* (Figure 14B, page 55). The large size (0.4Mb) of the 7qF3 locus might account for limited excision efficiency and mosaicism. At birth, when cortical angiogenesis is highly active, *16p11.2*^{Vasc} newborns displayed significantly reduced endothelial network branching in the cerebral cortex. Moreover, 16p11.2 haploinsufficient cECs displayed impaired sprouting, as evidenced by reduced density and length of filopodia extensions when compared to neighboring WT cECs (Figure 14B, page 55).

Gross cortical anatomy was assessed at P50. *16p11.2*^{Vasc} mice have normal cortical area

and thickness, as well as normal cortical layering (Figure 14C, page 55). However, NVC hemodynamics were measured in conditional *16p11.2*^{Vasc} mutants. NVC hemodynamics measured in conditional *16p11.2*^{Vasc} mutants showed similar defects as constitutive *16p11.2*$^{df/+}$mice (i.e. reduced response amplitude and slower kinetics) with the exception of baseline CBF, which remained at control values (Figure 15A, page 56). Also, as in *16p11.2*$^{df/+}$ mice, systolic blood pressure and heart rate were unaltered in *16p11.2*^{Vasc} mutants (Figure 15B, page 56). Therefore, an intact 16p11.2 (7qF3) locus is required for proper cerebrovascular maturation.

We observed that *16p11.2*^{Vasc} animals exhibit the expected home cage hyperactivity, especially in females (Figure 3B, page 37), while males displayed only a slight deficit during the first hours of habituation phase (Figure 3B, page 37). A striking and previously unknown feature of constitutive 16p11.2 deletion mice was a phenotype measured using the rotarod test. Indeed, a motor coordination impairment was evidenced in *16p11.2*^{Vasc} males, while better performances where measured in females, compared to sex-matched littermate controls (Figure 3D, page 37). In addition, *16p11.2*^{Vasc} males showed significantly increased marble burying, a common indicator of stereotypic and/or obsessive-compulsive behavior [160] (Figure 3F, page 37). However, both novel object recognition and social interaction (with vocalization recording) tests failed to reveal published phenotypes that are characteristic of 16p11.2 hemizygosity (Figure 3H-J, page 37).

Overall, this conditional (endothelial) mutation can recapitulate neurovascular dysfunction, structure abnormalities as well as ASD-like behaviors found in constitutive 16p11.2 deletion mutants. Thus, these findings demonstrate that endothelial 16p11.2 haploinsufficiency is sufficient to partially recapitulate 16p11.2-like behaviors.

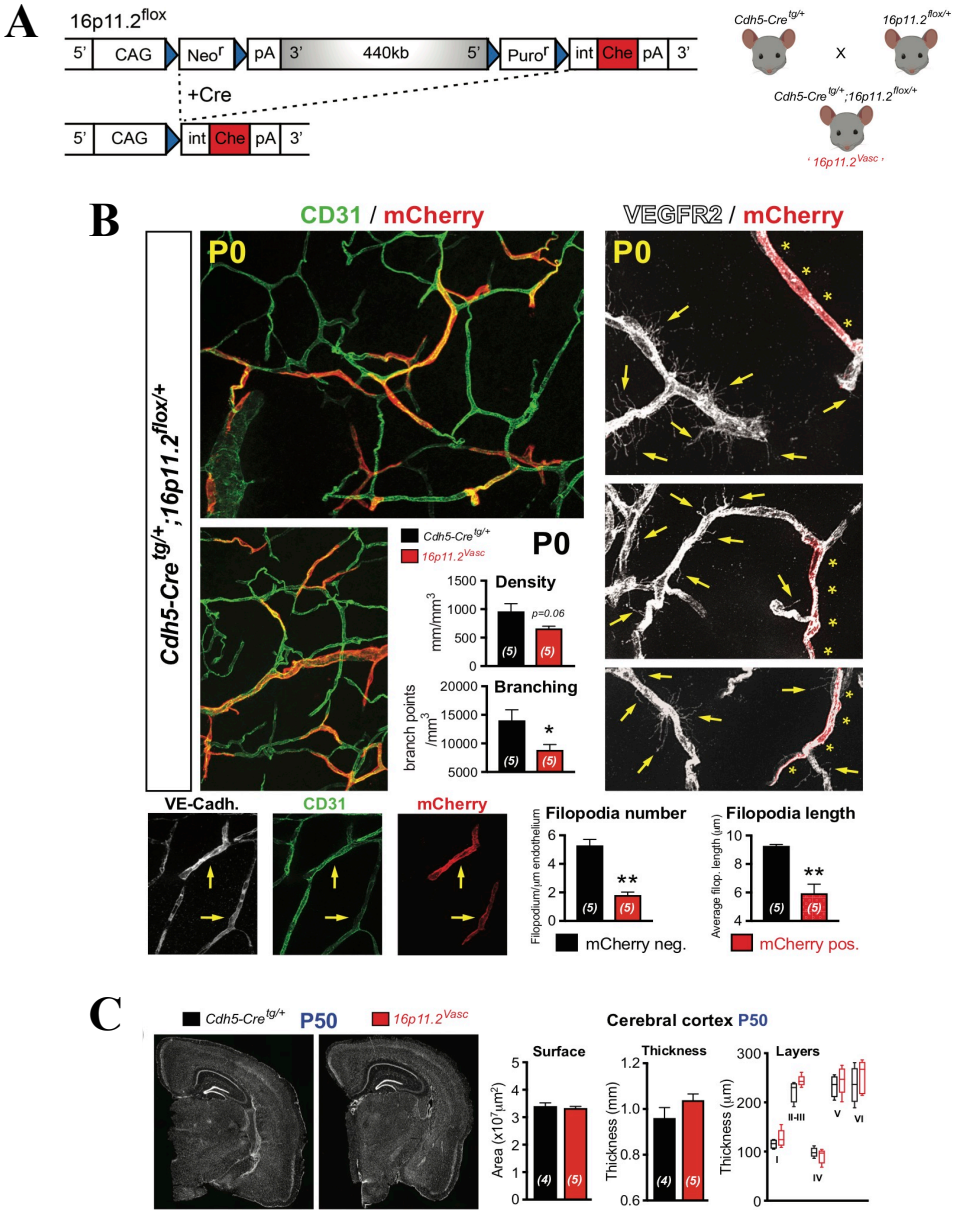

Figure 14. Cortical structure of endothelial-specific 16p11.2 haploinsufficiency mice.
(**A**) Schematic of mouse genetics and breeding strategy to obtain a specific endothelial deletion of the syntenic region of mouse locus 7qF3. **(B)** Immunohistochemical characterization of endothelial networks in the cerebral cortex at birth. *Top left images, 16p11.2^{Vasc}* newborns (P0), CD31/mCherry-double positive haploinsufficient cECs coexist with CD31-positive WT cECs in a mosaic. *Center graphs*, Quantifications of endothelial network density and branching at P0, showing significantly less branch points in *16p11.2^{Vasc}* animals than in control (*Cdh5-Cre$^{tg/+}$*) littermates. *Bottom left images* show expression of VE-Cadherin (*Cdh5* gene product) in CD31-positive cECs. *Top right images,* anti-VEGFR2/mCherry double immunostaining reveals that mCherry-positive haploinsufficient cECs (depicted by yellow stars) display less filopodia extensions, as quantified in bottom right graphs. **(C)** Micrographs of DAPI- stained brain sections. No differences were identified in total cortical surface, thickness, and layering at P50 between *16p11.2^{Vasc}* and control (*Cdh5-Cre$^{tg/+}$*) littermates. VE-Cadh, vascular endothelial cadherin. All data are mean ± s.e.m. (n=4-5 animals per group) $^{**}P < 0.01$ (Mann-Whitney test).

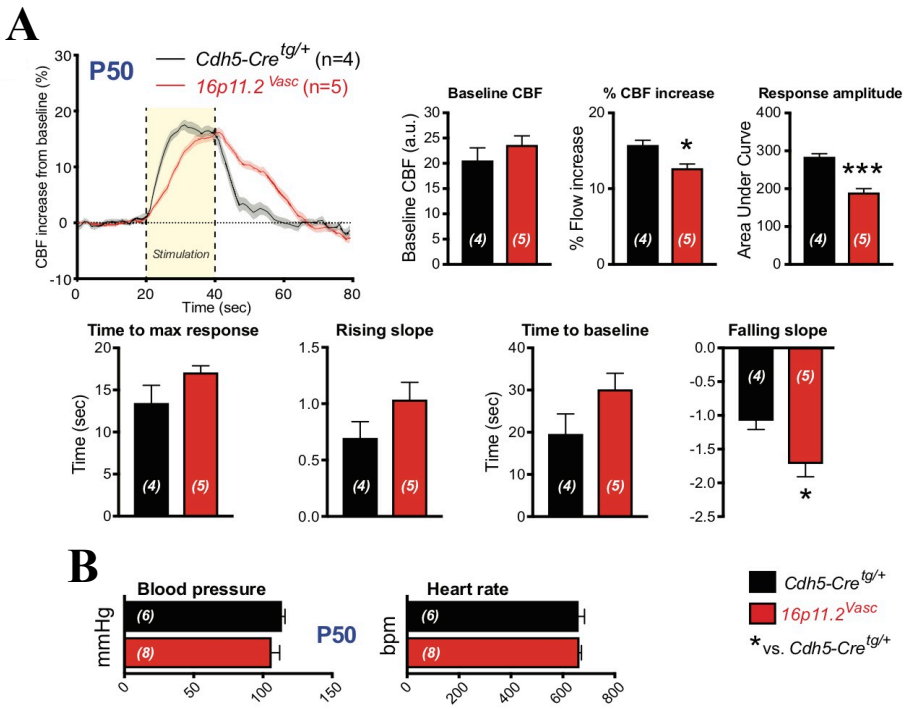

Figure 15. Activity-dependent regulation of cerebral blood flow (CBF) and systolic blood pressure in *16p11.2*^{Vasc} males.

(A) Laser Doppler flowmetry (LDF) coupled with whisker stimulation in anesthetized P50 male mice. Bar graphs represent hemodynamics parameters of CBF responses monitored over the primary somatosensory cortex. Adult 16p11.2^{Vasc} mice demonstrate a neurovascular coupling defect. **(B)** Mean systolic blood pressure and heart rate measured over 5 days at P50 using tail cuffs. WT, wild type. All data are the mean ± s.e.m (n=4-8 animals per group). *P < 0.05, ***P < 0.001 (Mann-Whitney test).

4. Discussion

4.1. Summary

Brain vasculature holds a great importance in maintaining normal brain development and function. Alterations in vascular function and/or structure can lead to severe health abnormalities such as neurological diseases. The present study sought to determine the role of defective cerebrovasculature in the pathophysiology of ASD. We studied cerebrovascular network structure and function in a rodent model of the 16p11.2 deletion syndrome, a well-known ASD mouse model. Haploinsufficiency at the 16p11.2 locus resulted in functional and structural vascular abnormalities, associated with cell-autonomous endothelial defects. Furthermore, we generated a model with endothelium-specific 16p11.2 haploinsufficiency, which displayed partial ASD-related behaviors, as well as similar functional abnormalities of the cerebrovasculature identified in the constitutive 16p11.2 deletion model. Our results demonstrate that endothelial cells are key contributors to the pathophysiology of the 16p11.2 deletion syndrome and provide a new framework to study neurodevelopmental disorders.

4.2. ASD-related behaviors in *16p11.2*$^{df/+}$ mice

In this study, we first assessed ASD-related behaviors in *16p11.2*$^{df/+}$ mice. We confirmed already-published behavioral data as these mice displayed abnormal known phenotypes in the beam break and novel object recognition tests [144, 146].

We report home-cage hyperactivity across the light-dark cycle that is present in both males and females. Our findings reproduce previous reports of hyperactivity in 16p11.2 deletion mice by comparing males and females, where home-cage activity was quantified over a week of consecutive diurnal cycles [145, 146]. The hyperactivity identified in these mice could potentially correlate to ADHD commonly associated with 16p11.2 deletion carriers [103].

In previously published studies, *16p11.2*$^{df/+}$ mice exhibited recognition memory deficits evidenced by a lack of interest for novel objects compared to WT mice. Impairment in the novel object recognition test suggest that mutant mice have difficulties in habituating to familiar objects which reflects behavioral inflexibility, a common characteristic reported in ASD patients [143, 144, 150]. Furthermore, ASD is associated with a preference for sameness and an aversion to novelty [161]. In our study we demonstrated that WT mice seek novelty, thus spending more time interacting with the novel object. Eventually, WT mice lose interest in familiar objects. However, *16p11.2*$^{df/+}$ males did not have a preference for the novel or familiar object which is indicative of a cognitive deficit and favors familiarity.

In published data these mice did not show motor coordination deficits on the rotarod, however it was only done over a two-day period [144, 145]. Here, we performed a long-term rotarod test lasting 7 days and identified significant differences between *16p11.2*$^{df/+}$ and WT mice when mice from both sexes were pooled. This difference could be attributed more to male mice, as they tend to perform slightly better overall. Male ASD children, in addition to being hyperactive, are capable of mastering a new skill with repetitive practice [162]. As this is a one-week test, it is a possibility that mutant mice are learning to perform better through repetition. However, we did not identify any deficits when assessing marble burying, behavior indicative of stereotypic movements. Other studies using this mouse model were able to identify stereotypic behaviors by observing jumping and climbing activity [143, 145].

This 16p11.2 deletion mouse model reproduces many behaviors found in human 16p11.2 deletion carriers, leading to a better understanding of ASD underpinnings, as well as sex-differences related to ASD symptomology. We also demonstrate behavioral differences between males and females. This observation is in line with reports suggesting that females could present

with ASD differently than males. Future studies are needed to identify the precise mechanisms of sex-specific differences in ASD prevalence/symptoms [163].

4.3. Abnormal endothelial function in *16p11.2*$^{df/+}$ mice

The majority of studies have focus on global cerebral perfusion when considering the vascular implications to ASD. ASD patient cohorts have demonstrated altered resting-state perfusion rates in different brain regions [61, 83, 85]. For instance, frontotemporal hyperperfusion has been identified in children and adolescents with ASD [85]. Reports have shown that adults diagnosed with ASD have elevated resting-state perfusion in the cerebral cortex as measured by arterial spin labeling-magnetic resonance imaging (ASL-MRI) [85]. In the present study, we measured resting-state perfusion in the cerebral cortex of a rodent model of 16p11.2 deletion syndrome using non-invasive ultrasound imaging. We demonstrated a higher baseline cerebral blood flow (CBF) in *16p11.2*$^{df/+}$ mice, which is in line with previous reports in humans. In addition, this result was further confirmed using LDF at P50, although no difference at P14 were identified in our mouse model.

Conventional blood oxygenation level dependent (BOLD) task-related fMRI and resting-state functional MRI (rs-fMRI) are capable of identifying areas of altered task-activity and changes of FC of brain networks [61]. We identified a reduced activity-dependent regulation of CBF in adult *16p11.2*$^{df/+}$ males. Again, this altered perfusion was in line with ASD patient data following task-induced MRI-BOLD signals in the cerebral cortex [31]. It is thought that these abnormalities are predictive of symptom severity [61]. Therefore, this brings to question if abnormal perfusion rates, more specifically resting perfusion rates, could serve as a biomarker for ASD. Interestingly, one study was able to accurately predict an ASD diagnosis using clinical MRI data from young infants[61], however not focusing on the vascular underpinnings of this imaging signal. Thus,

whether vascular abnormalities transpire before any obvious neuronal symptoms have yet to be elucidated. However, these results fortify the involvement of the brain vasculature to the symptoms presented in patients. Particularly, hypertension is a common characteristic identified in autism patients which could impact CBF [55]. However, in mice the elevated baseline CBF values were not attributed to increase arterial systolic blood pressure as seen between *16p11.2*$^{df/+}$ and WT males. These results suggest that the identified functional abnormalities are due to a central mechanism rather than to an altered cardiovascular function.

While we identified CBF abnormalities in males, females did not reveal any alterations via LDF measurements. Human studies that investigated brain perfusion in ASD patients did not consider sex differences in CBF [31, 61, 83, 85, 89]. Most studies have combined male and female data as an overall result as females are less-likely to be diagnosed with ASD. Therefore, information on comparison between males and females with ASD is lacking [85, 89]. Our study is the first step in filling this gap of knowledge, as we systematically compared male and female data for most of the readouts.

Moreover, fMRI data fails to provide a quantitative measurements of baseline metabolic activity. Using ASL-MRI, a study measured CBF as a surrogate of metabolic brain activity, as the vascular system was not the focus. The use of ASL-MRI to assess brain metabolism can be explained by comparable rates of perfusion and glucose uptake [85, 164]. As such, PET and SPECT studies in ASD patients have assessed baseline metabolic activity by quantifying the cerebral metabolic rate of glucose and cerebral blood flow (CBF) [89]. Baseline metabolic activity is another important index of resting brain function. Interestingly, research on glucose metabolism in ASD patients, especially in male individuals, demonstrated an increased global metabolism [89]. Following a glucose uptake assay, *16p11.2*$^{df/+}$ mice also displayed resting-state elevated glucose

uptake when compared to WT littermates. This suggest that adult *16p11.2*$^{df/+}$ mice may have an elevated glucose metabolism. This increase can indeed result from increased neuronal demands and/or an increase in glucose delivery by increased CBF in *16p11.2*$^{df/+}$ males. Interestingly, several studies have reported that ASD patients have increase brain metabolism [85]. Therefore, this response could be required to keep up with the increase cortical activity; however, the correlation has yet to be made. Although we identified an increase in glucose uptake, no difference was observed in blood oxygen saturation or total hemoglobin in the brain following photoacoustic imaging, suggesting that oxygen delivery and extraction is not altered in these mice, which is in favor of a vascular cause for our demonstration of increased FDG-PET signals in *16p11.2*$^{df/+}$ males. NVC is dependent on cerebrovascular integrity since CBF dysfunction is directly related to vasodilation and vasoconstriction responses [165]. To assess vascular reactivity and to exclude the influence of neural cells, we measured vasodilation and vasoconstriction responses *ex vivo*. This assay allowed us to determine if CBF dysregulation correlates with endothelial and/or smooth muscle cell dysfunction. Here, we identified endothelial cell dysfunction, whereby endothelium-dependent vasodilation was defective in isolated middle cerebral arteries (MCA) from P50 *16p11.2*$^{df/+}$ mice compared to WT littermates. In both MCAs and mesenteric arteries, smooth muscle cell function analysis using phenylephrine and exogenous NO, VSMCs were intact. Moreover, the mesenteric artery reproduced the impaired endothelial vasodilation response, hence confirming the endothelial nature of the deficits even outside the context of the brain. These findings demonstrate a close correlation between global CBF dysregulation and endothelial-specific impairments in mutant mice. From our knowledge, no study has ever looked at vascular reactivity without neuronal input in the context of ASD. Despite a report that assessed neurochemical control in neurovascular coupling by focusing on neurotransmitters and their effect

on blood flow, this report did not investigate vascular function as a contender to altered NVC in ASD [31]. In this thesis, we demonstrated an endothelial-specific defect which could explain the CBF dysregulation.

4.4. Developmental delay of endothelial network in *16p11.2*$^{df/+}$ mice

Endothelial cells are required to maintain normal brain function, especially in CBF regulation. Notably, during development, endothelial networks undergo remodeling. Angiogenesis was vaguely studied in ASD. One report evidenced that this process may persist for a longer period of time in the young ASD brain [71]. Here, we investigated endothelial development at two time points (P14 and P50), and identified a delay in endothelial development at P14 in three major subdivisions of the cerebral cortex in *16p11.2*$^{df/+}$ males. However, similar vascular branching and density at P50 between mutant and WT mice were evidenced, while the parietal cortex in layer IV displayed an elevated vascular density and branching in adult male mutants. This suggest that the endothelial network failed to undergo network remodeling as expected in this specific cortical region[24]. In addition, the delay in development at P14 followed by a normal endothelial network at P50 suggest that mutant males have an accelerated endothelial growth rate between these two ages. Furthermore, a discrepancy between structural and functional results is evidenced as unaltered CBF was identified at P14. Mutant females displayed similar patterns to WT females, also line with their normal CBF regulation. It is thus possible that accelerated rates of postnatal endothelial development in males led to an exhaustion of endothelial function at adulthood.

To assess if this phenotype was endothelial-specific, we investigated cells surrounding the endothelium *in vivo*. These cells (pericytes, astrocytes, VSMCs, microglia) closely interact with brain endothelial cells in the NVU to control cerebrovascular development and CBF [2, 30]. We identified normal assembly of the NVU, in addition to normal microglia development. From this

structural data, we can conclude that the early delay in endothelial network growth in *16p11.2*$^{df/+}$ cerebral cortex is endothelial-specific.

4.5. Impaired network forming abilities of *16p11.2*$^{df/+}$ endothelial cells

To further decipher the endothelial defects identified at the functional and structural level, we assessed brain endothelial network expansion and remodeling using isolated, primary cortical endothelial cells from P14 male mice (mutant and WT). Following an *in vitro* assay, we identified a severely impaired network forming/remodeling ability in *16p11.2*$^{df/+}$ cECs compared to WT cells. A possible explanation for this defect could have been that these cells were in a more proliferative state; however, following cell cycle analysis no difference was identified between WT and *16p11.2*$^{df/+}$ cECs, supporting the possibility of a defect in their angiogenic capacity.

Interestingly, 16p11.2-deletion endothelial cells isolated from mice revealed a cell autonomous defect as a consequence of 16p11.2 hemizygosity, which represent a novel finding.

4.6. Endothelial-specific 16p11.2 haploinsufficiency

The abnormalities evidenced endothelial-dependent vascular responses, vascular structure as well as angiogenesis brought us to investigate the contribution of endothelial cells to global ASD phenotypes. The impact of endothelial 16p11.2 haploinsufficiency on brain maturation and functions is unknown. To assess this knowledge gap, we generated mouse a model ('*16p11.2*^{Vasc}'mice) harboring the 16p11.2 deletion only in endothelial cells, using a genetic (CRE/lox) strategy. With similar assays as performed in constitutive *16p11.2*$^{df/+}$ mutants, we discovered that endothelial 16p11.2 haploinsufficiency was sufficient to trigger CBF and angiogenesis defects *in vivo*, as well as ASD-related mouse behaviors. Following structural analysis at birth, *16p11.2*^{vasc} mice revealed a mosaic pattern which allowed us to perform direct comparisons of WT and 16p11.2 haploinsufficient cECs *in vivo*. A possible explanation for the

identified mosaic endothelial network could be attributed to the large size of the 7qF3 locus, which might account for limited excision efficiency. Interestingly, at birth, *16p11.2*^{vasc} mice displayed a structural abnormality as revealed by reduced vascular branching. It is important to note that angiogenesis is highly active at birth [24], and the structural defect (i.e. reduced sprouting angiogenesis) was particularly evident at this age by assessment of filopodia extensions.

In the present study, we also assessed ASD-related behaviors in *16p11.2*^{Vasc} mice to investigate for the first time the contribution of endothelial cell-autonomous mutation to ASD-associated brain dysfunction. Humans carrying the 16p11.2 deletion display hyperactivity, stereotypic behaviors, impaired social interactions and difficulties with learning and motor skill development (16p11.2 Deletion Syndrome Guidebook, Simons VIP Connect, 2015), and we confirmed that such behaviors could be measured in constitutive *16p11.2*$^{df/+}$ mutants. The conditional "vascular" mutant mice demonstrated increased home-cage activity, increased marble burying and motor coordination deficits in males. However, not all behaviors associated with ASD were reproduced in this conditional model, as no deficits were identified in recognition memory as well as an absence in social interactions. These results suggest that the endothelial specific 16p11.2 deletion contributes ASD-associated brain dysfunction, but does not explain the full picture of this syndrome. However, more research is required to better understand specific vascular mechanisms that control these behavioral features, as it could lead to identification of novel therapeutic targets.

4.7. Sex-differences identified in 16p11.2 deletion mice

In this thesis, we identified various sex differences in behavior, functional and structural assays. The direct causes of these differences have yet to be determined. Previous studies have identified sex-specific differences in cerebrovascular biology[166]. For instance, women are

known to have an increase resting cerebral perfusion when compared to men as well as a higher perfusion rates during cognitive activity[167, 168]. Furthermore, reports have demonstrated that steroid hormones impact perfusion which may be a contributing factor to differences between men and women[167]. Specifically, testosterone and estradiol are known to alter vascular responses[167]. Interestingly, testosterone has vasoconstrictive effects while estradiol decreases vascular tone[167, 169]. Therefore, the differences identified in this study could be directly related to steroid hormones modulation. Additionally, autism spectrum disorders are more commonly found in males than females[163]. The reason behind the increase prevalence in males is unknown. However, theories have emerged suggesting that sex-differences in ASD are associated with women needing a bigger genetic burden to be diagnosed with these disorders and that estrogen has as a possible protective effect against ASD[58, 59, 170]. In this thesis the underlying causes of sex differences have not been determined. Thus, this avenue of research would be beneficial in order to understand male and female differences in ASD.

5. Conclusion

In this thesis, we investigated the endothelial contributions to ASD in a mouse model of the 16p11.2 deletion syndrome. Our findings demonstrate that endothelial-dependent vascular deficits are in part related to functional abnormalities found in 16p11.2 deletion carriers.

The present study establishes endothelial cells as key contributors to ASD and has identified new molecular players involved in this pathology. Future work is needed to decipher the mechanisms involved in the evidenced endothelial impairments. This study confirms that a healthy vasculature is required for proper brain development as well as supports literature on the higher prevalence of vascular-associated conditions in ASD patients. Indeed, our findings support previously identified vascular-associated comorbidities in ASD patients such as hypertension,

diabetes and stroke. Identifying the full contribution of vascular cells to the ASD pathology may lead to better strategies for prevention and early treatment.

This study identifies vascular abnormalities as contributors to ASD pathophysiology, and alters thinking on neuronal abnormalities as a sole source of ASD phenotypes. Further investigation is required to decipher the mechanisms involved in vascular links to ASD. Additionally, this thesis introduces new avenues to study neurodevelopmental disorders and further supports the importance of a well-established vasculature for proper brain function.

6. References

1. Deak, F., et al., *Recent Developments in Understanding Brain Aging: Implications for Alzheimer's Disease and Vascular Cognitive Impairment.* J Gerontol A Biol Sci Med Sci, 2016. **71**(1): p. 13-20.
2. Andreone, B.J., B. Lacoste, and C. Gu, *Neuronal and vascular interactions.* Annu Rev Neurosci, 2015. **38**: p. 25-46.
3. Attwell, D.a. and S. Laughlin, *An Energy Budget for Signaling in the Grey Matter of the Brain.* Journal of Cerebral Blood Flow and Metabolism, 2001. **21**: p. 1133-1145.
4. Peters, A., et al., *The selfish brain: competition for energy resources.* Neurosci Biobehav Rev, 2004. **28**(2): p. 143-80.
5. Lacoste, B. and C. Gu, *Control of cerebrovascular patterning by neural activity during postnatal development.* Mech Dev, 2015. **138 Pt 1**: p. 43-9.
6. Girouard, H. and C. Iadecola, *Neurovascular coupling in the normal brain and in hypertension, stroke, and Alzheimer disease.* J Appl Physiol (1985), 2006. **100**(1): p. 328-35.
7. Quaegebeur, A., C. Lange, and P. Carmeliet, *The neurovascular link in health and disease: molecular mechanisms and therapeutic implications.* Neuron, 2011. **71**(3): p. 406-24.
8. Huneau, C., H. Benali, and H. Chabriat, *Investigating Human Neurovascular Coupling Using Functional Neuroimaging: A Critical Review of Dynamic Models.* Frontiers in Neuroscience, 2015. **9**(467).
9. Lecrux, C. and E. Hamel, *The neurovascular unit in brain function and disease.* Acta Physiol (Oxf), 2011. **203**(1): p. 47-59.
10. Attwell, D., et al., *Glial and neuronal control of brain blood flow.* Nature, 2010. **468**(7321): p. 232-43.
11. De Filippis, L. and D. Delia, *Hypoxia in the regulation of neural stem cells.* Cell Mol Life Sci, 2011. **68**(17): p. 2831-44.
12. Stone, J., et al., *Development of Retinal Vasculature Is Mediated by Hypoxia- Induced Vascular Endothelial Growth Factor (VEGF) Expression by Neuroglia.* The Journal of Neuroscience, 1995. **15**(7): p. 4738-4747.
13. Tata, M. and C. Ruhrberg, *Cross-talk between blood vessels and neural progenitors in the developing brain.* Neuronal Signaling, 2018.
14. Hogan, K.A., et al., *The neural tube patterns vessels developmentally using the VEGF signaling pathway.* Development, 2004. **131**(7): p. 1503-13.
15. Daneman, R., et al., *Wnt/ -catenin signaling is required for CNS, but not non-CNS, angiogenesis.* PNAS, 2009. **106**(2): p. 641-646.
16. James, J.M., C. Gewolb, and V.L. Bautch, *Neurovascular development uses VEGF-A signaling to regulate blood vessel ingression into the neural tube.* Development, 2009. **136**(5): p. 833-41.
17. Carmeliet, P. and R.K. Jain, *Molecular mechanisms and clinical applications of angiogenesis.* Nat Review, 2011. **473**: p. 298-307.
18. Li, S., et al., *Endothelial VEGF Sculpts Cortical Cytoarchitecture.* The Journal of Neuroscience, 2013. **33**(37): p. 14809-14815.
19. Butler, J.M., H. Kobayashi, and S. Rafii, *Instructive role of the vascular niche in promoting tumour growth and tissue repair by angiocrine factors.* Nat Rev Cancer, 2010. **10**(2): p. 138-46.

20. Lee, S., et al., *Autocrine VEGF Signaling Is Required for Vascular Homeostasis.* Cell, 2007. **130**: p. 691-703.
21. Kozberg, M.G., et al., *Rapid Postnatal Expansion of Neural Networks Occurs in an Environment of Altered Neurovascular and Neurometabolic Coupling.* J Neurosci, 2016. **36**(25): p. 6704-17.
22. Yamada, H., et al., *A milestone for normal development of the infantile brain detected by functional MRI.* Neurology, 2000. **55**: p. 218-223.
23. Muramuto, S., et al., *Age-dependent change in metabolic re- sponse to photic stimulation of the primary visual cortex in infants: functional mag- netic resonance imaging study.* J. Comput. Assist. Tomogr., 2002. **26**: p. 894-901.
24. Lacoste, B., et al., *Sensory-Related Neural Activity Regulates the Structure of Vascular Networks in the Cerebral Cortex.* Neuron, 2014. **83**(5): p. 1117-1130.
25. Ballabh, P., A. Braun, and M. Nedergaard, *The blood-brain barrier: an overview: structure, regulation, and clinical implications.* Neurobiol Dis, 2004. **16**(1): p. 1-13.
26. Hawkins, B.T. and T.P. Davis, *The blood-brain barrier/neurovascular unit in health and disease.* Pharmacol Rev, 2005. **57**(2): p. 173-85.
27. Mergenthaler, P., et al., *Sugar for the brain: the role of glucose in physiological and pathological brain function.* Trends Neurosci, 2013. **36**(10): p. 587-97.
28. Frosen, J. and A. Joutel, *Smooth muscle cells of intracranial vessels: from development to disease.* Cardiovasc Res, 2018. **114**(4): p. 501-512.
29. Armulik, A., et al., *Pericytes regulate the blood-brain barrier.* Nature, 2010. **468**(7323): p. 557-61.
30. Daneman, R., et al., *Pericytes are required for blood-brain barrier integrity during embryogenesis.* Nature, 2010. **468**(7323): p. 562-6.
31. Reynell, C. and J.J. Harris, *The BOLD signal and neurovascular coupling in autism.* Dev Cogn Neurosci, 2013. **6**: p. 72-9.
32. Sandoo, A., et al., *The Endothelium and Its Role in Regulating Vascular Tone.* The open cardiovascular medicine journal, 2010. **4**: p. 302-312.
33. Bergers, G. and S. Song, *The role of pericytes in blood-vessel formation and maintenance.* Neuro Oncol, 2005. **7**(4): p. 452-64.
34. Arnold, T. and C. Betsholtz, *The importance of microglia in the development of the vasculature in the central nervous system.* Vascular Cell, 2013. **5**(4).
35. Sweeney, M.D., et al., *The role of brain vasculature in neurodegenerative disorders.* Nat Neurosci, 2018. **21**(10): p. 1318-1331.
36. Ruhrberg, C. and V.L. Bautch, *Neurovascular development and links to disease.* Cell. Mol. Life Sci., 2013. **70**: p. 1675-1684.
37. Hu, X., et al., *Cerebral Vascular Disease and Neurovascular Injury in Ischemic Stroke.* Circ Res, 2017. **120**(3): p. 449-471.
38. Chen, J.J., D.H. Salat, and H.D. Rosas, *Complex relationships between cerebral blood flow and brain atrophy in early Huntington's disease.* Neuroimage, 2012. **59**(2): p. 1043-51.
39. Van Dyken, P. and B. Lacoste, *Impact of Metabolic Syndrome on Neuroinflammation and the Blood*–Brain Barrier. Frontiers in Neuroscience, 2018. 1**2.**
40. Jack, C.R., et al., *Tracking pathophysiologicalprocesses in Alzheimer's disease:* an updated hypothetical model of dynamic biomarkers. Lancet Neurol, 2013. **12**: p. 207-216.

41. Arvanitakis, Z., et al., *Relation of cerebral vessel disease to Alzheimer's disease dementia and cognitive function in elderly people: a cross-sectional study.* Lancet Neurol, 2016. 15: p. 934-943.
42. Leeuwis, A.E., et al., *Lower cerebral blood flow is associated with impairment in multiple cognitive domains in Alzheimer's disease.* Alzheimers Dement, 2017. **13**(5): p. 531-540.
43. Kisler, K., et al., *Pericyte degeneration leads to neurovascular uncoupling and limits oxygen supply to brain.* Nat Neurosci, 2016. **20**(3): p. 406-420.
44. Montagne, A., et al., *Brain imaging of neurovascular dysfunction in Alzheimer's disease.* Acta Neuropathol, 2016. **131**(5): p. 687-707.
45. Chen, Y., et al., *Voxel-level comparison of arterial spin-labeled perfusion MRI and FDG-PET in Alzheimer disease.* Neurology, 2011. **77**(22): p. 1977-1985.
46. Small, S.A., et al., *Differential Regional Dysfunction of the Hippocampal Formation among Elderly with Memory Decline and Alzheimer's Disease. Ann. Neurol, 1999. 45*: p. 466-472.
47. Rombouts, S., et al., *Functional MR Imaging in Alzheimer's Disease during Memory Encoding.* Am J Neuroradiol, 2000. 21: p. 1869-1875.
48. Hillman, E.M., *Coupling mechanism and significance of the BOLD signal: a status report.* Annu Rev Neurosci, 2014. **37**: p. 161-81.
49. Montagne, A., et al., *Blood-brain barrier breakdown in the aging human hippocampus.* Neuron, 2015. **85**(2): p. 296-302.
50. Syrimi, Z.J., et al., *Arterial spin labelling detects posterior cortical hypoperfusion in non-demented patients with Parkinson's disease.* J Neural Transm (Vienna), 2017. **124**(5): p. 551-557.
51. Rule, R.R., et al., *Gray matter perfusion correlates with disease severity in ALS.* Neurology, 2010. **74**(10): p. 821-827.
52. Zlokovic, B.V., *The blood-brain barrier in health and chronic neurodegenerative disorders.* Neuron, 2008. **57**(2): p. 178-201.
53. Joutel, A., *Pathogenesis of CADASIL: transgenic and knock-out mice to probe function and dysfunction of the mutated gene, Notch3, in the cerebrovasculature.* Bioessays, 2011. **33**(1): p. 73-80.
54. Vijayakumar, N.T. and M.V. Judy, *Autism spectrum disorders: Integration of the genome, transcriptome and the environment.* J Neurol Sci, 2016. **364**: p. 167-76.
55. Croen, L.A., et al., *The health status of adults on the autism spectrum.* Autism, 2015. **19**(7): p. 814-23.
56. Park, H.R., et al., *A Short Review on the Current Understanding of Autism Spectrum Disorders.* Exp Neurobiol, 2016. **25**(1): p. 1-13.
57. Grissom, N.M., et al., *Male-specific deficits in natural reward learning in a mouse model of neurodevelopmental disorders.* Mol Psychiatry, 2018. **23**(3): p. 544-555.
58. Jacquemont, S., et al., *A higher mutational burden in females supports a "female protective model" in neurodevelopmental disorders.* Am J Hum Genet, 2014. **94**(3): p. 415-25.
59. Robinson, E.B., et al., *Examining and interpreting the female protective effect against autistic behavior.* Proc Natl Acad Sci U S A, 2013. **110**(13): p. 5258-62.
60. Amendah, D., et al., *The economic costs of autism: a review.*Oxford University Press, 2012.
61. Emerson, R.W., et al., *Functional neuroimaging of high-risk 6-month-old infants predicts a diagnosis of autism at 24 months of age.* Sci Transl Med, 2017. **9**(393): p. eaag2882.

62. Lord, C., et al., *Autism From 2 to 9 Years of Age.* Arch Gen Psychiatry, 2006. **63**(6): p. 694-701.
63. Kim, H., C.S. Lim, and B.K. Kaang, *Neuronal mechanisms and circuits underlying repetitive behaviors in mouse models of autism spectrum disorder.* Behav Brain Funct, 2016. **12**(1): p. 3.
64. Lyall, K., et al., *The Changing Epidemiology of Autism Spectrum Disorders.* Annu Rev Public Health, 2017. **38**: p. 81-102.
65. Kanner, L., *Autistic Disturbances of Affective Contact.* Acta Paedopsychiatr., 1968. **35**(4): p. 100-36.
66. Greco, B., et al., *Autism-related behavioral abnormalities in synapsin knockout mice.* Behav Brain Res, 2013. **251**: p. 65-74.
67. Peca, J., et al., *Shank3 mutant mice display autistic-like behaviours and striatal dysfunction.* Nature, 2011. **472**(7344): p. 437-42.
68. Kozol, R.A., et al., *Two knockdown models of the autism genes SYNGAP1 and SHANK3 in zebrafish produce similar behavioral phenotypes associated with embryonic disruptions of brain morphogenesis.* Hum Mol Genet, 2015. **24**(14): p. 4006-23.
69. Zhang, J., et al., *Association of NCAM1 polymorphisms with autism and parental age at conception in a Chinese Han population.* Genet Test Mol Biomarkers, 2014. **18**(10): p. 690-4.
70. Lin, Y.C., et al., *A Subset of Autism-Associated Genes Regulate the Structural Stability of Neurons.* Frontiers in Neuroscience, 2016. **10**(263).
71. Azmitia, E.C., et al., *Persistent Angiogenesis in the Autism Brain: An Immunocytochemical Study of Postmortem Cortex, Brainstem and Cerebellum.* J Autism Dev Disord, 2016. **46**(4): p. 1307-18.
72. Courchesne, E.C., R. Akshoomoff, N., *Evidence of brain overgrowth in the first year of life in autism.* JAMA, 2003. **290**(3): p. 337-44.
73. Ebert, D.H. and M.E. Greenberg, *Activity-dependent neuronal signalling and autism spectrum disorder.* Nature, 2013. **493**(7432): p. 327-37.
74. Bosl, W.J., H. Tager-Flusberg, and C.A. Nelson, *EEG Analytics for Early Detection of Autism Spectrum Disorder: A data-driven approach.* Sci Rep, 2018. **8**(1): p. 6828.
75. Fatemi, S.H., et al., *Glutamic acid decarboxylase 65 and 67 kDa proteins are reduced in autistic parietal and cerebellar cortices.* Biological Psychiatry, 2002. **52**(8): p. 805-810.
76. Purcell, A.E., et al., *Postmortem brain abnormalities of the glutamate neurotransmitter system in autism.* Neurology, 2001. **57**: p. 1618-1628.
77. Takarae, Y. and J. Sweeney, *Neural Hyperexcitability in Autism Spectrum Disorders*. Brain Sci, 2017. **7**(10).
78. Kaushik, G. and K.S. Zarbalis, *Prenatal Neurogenesis in Autism Spectrum Disorders.* Frontiers in Chemistry, 2016. **4**(12).
79. Courchesne, E., et al., *Neuron Number and Size in Prefrontal Cortex of Children With Autism.* JAMA, 2011. **306**: p. 2001-2010.
80. Donovan, A.P. and M.A. Basson, *The neuroanatomy of autism - a developmental perspective.* J Anat, 2017. **230**(1): p. 4-15.
81. Fang, W.-Q., et al., *Overproduction of Upper-Layer Neurons in the Neocortex Leads to Autism-like Features in Mice.* Cell Rep, 2014. **9**: p. 1635-1643.
82. Tang, G., et al., *Loss of mTOR-dependent macroautophagy causes autistic-like synaptic pruning deficits.* Neuron, 2014. **83**(5): p. 1131-43.

83. Gupta, S.K.R., B.V., *Cerebral perfusion abnormalities in children with autism and mental retardation: a segmental quantitative SPECT study.* Indian Pediatr., 2009. **46**(2): p. 161-4.
84. Faraci, F.M., *Protecting against vascular disease in brain.* Am J Physiol Heart Circ Physiol, 2011. **300**(5): p. H1566-82.
85. Jann, K., et al., *Altered resting perfusion and functional connectivity of default mode network in youth with autism spectrum disorder.* Brain Behav, 2015. **5**(9): p. e00358.
86. Zilbovicius, M., et al., *Temporal Lobe Dysfunction in Childhood Autism: A PET Study.* Am J Psychiatry, 2000. **157**: p. 1988-1993.
87. Ito, H., et al., *Findings of brain 99mTc-ECD SPECT in high-functioning autism - 3-dimensional stereotactic ROI template analysis of brain SPECT -.* J Med Invest. , 2005. **52**(1-2): p. 49-56.
88. Degirmenci, B., et al., *Technetium-99m HMPAO brain SPECT in autistic children and their families.* Psychiatry Res, 2008. **162**(3): p. 236-43.
89. Yang, W.H., et al., *Regional cerebral blood flow in children with autism spectrum disorders: a quantitative ^{99}mTc-ECD brain SPECT study with statistical parametric mapping evaluation. Chin Med J (Engl). 2011. 124(9): p. 1362-6.*
90. Kaya, M., et al., *The relationship between 99mTc-HMPAO brain SPECT and the scores of real life rating scale in autistic children.* Brain Dev., 2002. **24**(2): p. 77-81.
91. Burroni, L., et al., *Regional cerebral blood flow in childhood autism: a SPET study with SPM evaluation.* Nucl Med Commun., 2008. **29**(2): p. 150-6.
92. Mountz, J., et al., *Functional deficits in autistic disorder: characterization by technetium-99m-HMPAO and SPECT. J* Nucl Med., 1995. *3***6**(7): p. 1156-62.
93. George, M., et al., *Cerebral Blood Flow Abnormalities in Adults with Infantile Autism.* J Nerv Ment Dis., 1992. **180**(7): p. 413-7.
94. Ohnishi , T., et al., *Abnormal regional cerebral blood flow in childhood autism.* Brain, 2000. **123**(Pt 9): p. 1838-44.
95. Tarlungeanu, D.C., et al., *Impaired Amino Acid Transport at the Blood Brain Barrier Is a Cause of Autism Spectrum Disorder.* Cell, 2016. **167**(6): p. 1481-1494 e18.
96. Hanson, E., et al., *Cognitive and behavioral characterization of 16p11.2 deletion syndrome.* J Dev Behav Pediatr, 2010. **31**(8): p. 649-57.
97. Griesi-Oliveira, K. and A. Laurato Sertié, *Autism spectrum disorders: an updated guide for genetic counseling.* einstein, 2017. **15**(2): p. 233-8.
98. Sebat, J., et al., *Strong association of de novo copy number mutations with autism.* Science, 2007. **316**(5823): p. 445-9.
99. Gazzellone, M., et al., *Copy number variation in Han Chinese individuals with autism spectrum disorder.* J Neurodev Disord 2014. **6**(1).
100. Cook, E.H., Jr. and S.W. Scherer, *Copy-number variations associated with neuropsychiatric conditions.* Nature, 2008. **455**(7215): p. 919-23.
101. Blumenthal, I., et al., *Transcriptional consequences of 16p11.2 deletion and duplication in mouse cortex and multiplex autism families.* Am J Hum Genet, 2014. **94**(6): p. 870-83.
102. Marshall, C.R., et al., *Structural variation of chromosomes in autism spectrum disorder.* Am J Hum Genet, 2008. **82**(2): p. 477-88.
103. Shinawi, M., et al., *Recurrent reciprocal 16p11.2 rearrangements associated with global developmental delay, behavioural problems, dysmorphism, epilepsy, and abnormal head size.* J Med Genet, 2010. **47**(5): p. 332-41.

104. Steinberg, S., et al., *Common variant at 16p11.2 conferring risk of psychosis.* Molecular Psychiatry, 2012. **19**(1): p. 108-114.
105. Fernandez, B.A., et al., *Phenotypic spectrum associated with de novo and inherited deletions and duplications at 16p11.2 in individuals ascertained for diagnosis of autism spectrum disorder.* J Med Genet, 2010. **47**(3): p. 195-203.
106. Degenhardt, F., et al., *Identification of rare variants in KCTD13 at the schizophrenia risk locus 16p11.2.* Psychiatr Genet, 2016. **26**(6): p. 293-296.
107. Kirov, G., *CNVs in neuropsychiatric disorders.* Hum Mol Genet, 2015. **24**(R1): p. R45-9.
108. Zheng, X., et al., *The association between rare large duplication of 16p11.2 and schizophrenia in the Singaporean Chinese population.* Schizophr Res, 2013. **146**(1-3): p. 368-9.
109. Kumar, R.A., et al., *Recurrent 16p11.2 microdeletions in autism.* Human Molecular Genetics, 2007. **17**(4): p. 628-638.
110. Weiss, L., et al., *Association between Microdeletion and Microduplication at 16p11.2 and Autism.* N Engl J Med, 2008. **358**(7): p. 667-75.
111. Rosenfeld, J.A., et al., *Copy number variations associated with autism spectrum disorders contribute to a spectrum of neurodevelopmental disorders.* Genet Med, 2010. **12**(11): p. 694-702.
112. Bijlsma, E.K., et al., *Extending the phenotype of recurrent rearrangements of 16p11.2: deletions in mentally retarded patients without autism and in normal individuals.* Eur J Med Genet, 2009. **52**(2-3): p. 77-87.
113. Qureshi, A.Y., et al., *Opposing brain differences in 16p11.2 deletion and duplication carriers.* J Neurosci, 2014. **34**(34): p. 11199-211.
114. Owen, J.P., et al., *Brain MR Imaging Findings and Associated Outcomes in Carriers of the Reciprocal Copy Number Variation at 16p11.2.* Radiology, 2018. **286**(1): p. 217-226.
115. Dell'Edera, D., et al., *16p11.2 microdeletion syndrome: a case report.* J Med Case Rep, 2018. **12**(1): p. 90.
116. Ryu, S. and S. Park, *Targeting major vault protein in senescence-associated apoptosis resistance.* Expert Opin Ther Targets 2009. **13**(4): p. 479-84.
117. Mamczur, P., et al., *Nuclear localization of aldolase A correlates with cell proliferation.* . Biochim Biophys Acta, 2013. **1833**(12): p. 2812-22.
118. Ojeda, V., A. Castro-Castro, and X. Bustelo, *Coronin1 proteins dictate rac1 intracellular dynamics and cytoskeletal output.* . Mol Cell Biol, 2014. **34**(18): p. 3388-406.
119. Golzio, C., et al., *KCTD13 is a major driver of mirrored neuroanatomical phenotypes of the 16p11.2 copy number variant.* Nature, 2012. **485**(7398): p. 363-7.
120. Takemoto, T., et al., *Tbx6-dependent Sox2 regulation determines neural or mesodermal fate in axial stem cells.* Nature, 2011. **470**(7334): p. 394-8.
121. Yadav, S., et al., *TAOK2 Kinase Mediates PSD95 Stability and Dendritic Spine Maturation through Septin7 Phosphorylation.* . Neuron, 2017. **93**(2): p. 379-93.
122. Gladwyn-Ng, I., et al., *Bacurd1/Kctd13 and Bacurd2/Tnfaip1 are interacting partners to Rnd proteins which influence the long-term positioning and dendritic maturation of cerebral cortical neurons.* . Neural development 2016. **11**(7).
123. Xie, Y., et al., *The phosphatase PP4c controls spindle orientation to maintain proliferative symmetric divisions in the developing neocortex.* . Neuron, 2013. **79**(2): p. 254-65

124. Park, S.M., H.R. Park, and J.H. Lee, *MAPK3 at the Autism-Linked Human 16p11.2 Locus Influences Precise Synaptic Target Selection at Drosophila Larval Neuromuscular Junctions.* Mol Cells, 2017. **40**(2): p. 151-161.
125. Mochida, S., et al., *Mochida S, Orita S, Sakaguchi G, Sasaki T, Takai Y. Role of the Doc2 alpha-Munc13-1 interaction in the neurotransmitter release process.* . Proc Natl Acad Sci U S A 1998. **95**(19): p. 11418-22.
126. Valente, P., et al., *PRRT2 Is a Key Component of the Ca(2+)-Dependent Neurotransmitter Release Machinery.* . Cell Rep, 2016. **15**(1): p. 117-31.
127. Valtorta, F., et al., *PRRT2: from Paroxysmal Disorders to Regulation of Synaptic Function.* . Trends Neurosci, 2014. **39**(10): p. 668-79.
128. Yao, J., et al., *Doc2 is a Ca2+ sensor required for asynchronous neurotransmitter release.* Cell, 2011. **147**(3): p. 666-77.
129. Mody, M. and J.W. Belliveau, *Speech and Language Impairments in Autism: Insights from Behavior and Neuroimaging.* N Am J Med Sci, 2013. **5**(3): p. 157-161.
130. Ellis Weismer, S., C. Lord, and A. Esler, *Early language patterns of toddlers on the autism spectrum compared to toddlers with developmental delay.* J Autism Dev Disord, 2010. **40**(10): p. 1259-73.
131. Zufferey, F., et al., *A 600 kb deletion syndrome at 16p11.2 leads to energy imbalance and neuropsychiatric disorders.* J Med Genet, 2012. **49**(10): p. 660-8.
132. Owen, J.P., et al., *Aberrant white matter microstructure in children with 16p11.2 deletions.* J Neurosci, 2014. **34**(18): p. 6214-23.
133. Blackmon, K., et al., *Focal Cortical Anomalies and Language Impairment in 16p11.2 Deletion and Duplication Syndrome.* Cerebral Cortex, 2018. **28**(7): p. 2422-2430.
134. Zhang, Y., et al., *An RNA-sequencing transcriptome and splicing database of glia, neurons, and vascular cells of the cerebral cortex.* . J Neurosci, 2014. **34**(36): p. 11929-47.
135. Meadows KN, Bryant P, and P. K., *Vascular endothelial growth factor induction of the angiogenic phenotype requires Ras activation.* . J Biol Chem, 2001. **276**(52): p. 49289-98.
136. Srinivasan R, et al., *Erk1 and Erk2 regulate endothelial cell proliferation and migration during mouse embryonic angiogenesis.* PLoS One, 2009. **4**(12): p. e8283.
137. Shin M, et al., *Vegfa signals through ERK to promote angiogenesis, but not artery differentiation.* . Development, 2016. **143**(20): p. 3796-805.
138. Andrikopoulos P, Eccles SA, and Y. MM., *Coupling between the TRPC3 ion channel and the NCX1 transporter contributed to VEGF-induced ERK1/2 activation and angiogenesis in human primary endothelial cells.* Cellular signalling, 2017(37): p. 12-30.
139. Yu Z, et al., *Erianin inhibits high glucose-induced retinal angiogenesis via blocking ERK1/2-regulated HIF-1alpha-VEGF/VEGFR2 signaling pathway.* . Sci Rep, 2016(6): p. 34306.
140. Zhang Q, Soderland C, and S. JJ., *Regulation of retinal endothelial cell apoptosis through activation of the IGFBP-3 receptor* Apoptosis : an international journal on programmed cell death 2013. **18**(3): p. 361-8.
141. Smits M, et al., *Myc-associated zinc finger protein (MAZ) is regulated by miR-125b and mediates VEGF-induced angiogenesis in glioblastoma.* FASEB journal : official publication of the Federation of American Societies for Experimental Biology 2012. **26**(6): p. 2639-47.
142. Ray A and R. BK, *Induction of Ras by SAF-1/MAZ through a feed-forward loop promotes angiogenesis in breast cancer* Cancer Med, 2015. **4**(2): p. 224-34.

143. Horev, G., et al., *Dosage-dependent phenotypes in models of 16p11.2 lesions found in autism.* Proc Natl Acad Sci U S A, 2011. **108**(41): p. 17076-81.
144. Portmann, T., et al., *Behavioral abnormalities and circuit defects in the basal ganglia of a mouse model of 16p11.2 deletion syndrome.* Cell Rep, 2014. **7**(4): p. 1077-1092.
145. Arbogast, T., et al., *Reciprocal Effects on Neurocognitive and Metabolic Phenotypes in Mouse Models of 16p11.2 Deletion and Duplication Syndromes.* PLoS Genet, 2016. **12**(2): p. e1005709.
146. Angelakos, C.C., et al., *Hyperactivity and male-specific sleep deficits in the 16p11.2 deletion mouse model of autism.* Autism Res, 2017. **10**(4): p. 572-584.
147. Yang, M., et al., *16p11.2 Deletion Syndrome Mice Display Sensory and Ultrasonic Vocalization Deficits During Social Interactions.* Autism Res, 2015. **8**(5): p. 507-21.
148. Tian, D., et al., *Contribution of mGluR5 to pathophysiology in a mouse model of human chromosome 16p11.2 microdeletion.* Nat Neurosci, 2015. **18**(2): p. 182-185.
149. Alva JA, et al., *VE-Cadherin-Cre-recombinase transgenic mouse: a tool for lineage analysis and gene deletion in endothelial cells.* Dev Dyn, 2006. **253**(3): p. 759-67.
150. Simons Vip, C., *Simons Variation in Individuals Project (Simons VIP): a genetics-first approach to studying autism spectrum and related neurodevelopmental disorders.* Neuron, 2012. **73**(6): p. 1063-7.
151. Lacoste, B., et al., *Cognitive and cerebrovascular improvements following kinin B1 receptor blockade in Alzheimer's disease mice.* Journal of Neuroinflammation, 2013. **10**(57).
152. Chen, B., et al., *High-speed vascular dynamics of the hemodynamic response.* Neuroimage, 2011. **54**: p. 1021-1030.
153. Thibodeau, J.F., et al., *Vascular Smooth Muscle-Specific EP4 Receptor Deletion in Mice Exacerbates Angiotensin II-Induced Renal Injury.* Antioxid Redox Signal, 2016. **25**(12): p. 642-656.
154. Tremblay, M.E., M. Riad, and A. Majewska, *Preparation of mouse brain tissue for immunoelectron microscopy.* J Vis Exp, 2010(41).
155. Bisht, K., et al., *Correlative Light and Electron Microscopy to Study Microglial Interactions with beta-Amyloid Plaques.* J Vis Exp, 2016(112).
156. Cao, V.Y., et al., *Motor Learning Consolidates Arc-Expressing Neuronal Ensembles in Secondary Motor Cortex.* Neuron, 2015. **86**(6): p. 1385-92.
157. Behringer, R., et al., *Selecting Female Mice in Estrus and Checking Plugs.* Cold Spring Harb Protoc, 2016. **2016**(8).
158. Angoa-Pérez, M., et al., *Marble Burying and Nestlet Shredding as Tests of Repetitive, Compulsive-like Behaviors in Mice.* J. Vis. Exp., 2013(82): p. e50978.
159. Bowers, K.J., et al., *Cerebrovascular disease in children: recent advances in diagnosis and management.* J Child Neurol, 2011. **26**(9): p. 1074-100.
160. Silverman, J.L., et al., *Behavioural phenotyping assays for mouse models of autism.* Nat Rev Neurosci, 2010. **11**: p. 490-502.
161. Keehn, B., R.A. Muller, and J. Townsend, *Atypical attentional networks and the emergence of autism.* Neurosci Biobehav Rev, 2013. **37**(2): p. 164-83.
162. Parsons, S. and P. Mitchell, *The potential of virtual reality in social skills training for people with autistic spectrum disorders.* Journal of Intellectual Disability Research, 2002. **46**: p. 430-443.

163. Lai, M.C., et al., *A behavioral comparison of male and female adults with high functioning autism spectrum conditions.* PLoS One, 2011. **6**(6): p. e20835.
164. Zimmer, E.R., et al., *[(18)F]FDG PET signal is driven by astroglial glutamate transport.* Nat Neurosci, 2017. **20**(3): p. 393-395.
165. Sestini, S., A. Castagnoli, and L. Mansi, *The new FDG brain revolution: the neurovascular unit and the default network.* Eur J Nucl Med Mol Imaging, 2010. **37**(5): p. 913-6.
166. McCarthy, M., et al., *Sex differences in the brain: the not so inconvenient truth.* J Neurosci, 2008. **32**(7): p. 2241-7.
167. Ghisleni C, Bollmann S, and B.-L. A, *Effects of Steroid Hormones on Sex Differences in Cerebral Perfusion.* PLoS One, 2015. **10**(9): p. e0135827.
168. Gur RC, Gur RE, and O. WD, *Sex and handedness differences in cerebral blood flow during rest and cognitive activity.* Science, 1982. **217**(4560): p. 659-61.
169. Ospina JA, Duckles SP, and Krause DN, *17beta-estradiol decreases vascular tone in cerebral arteries by shifting COX-dependent vasoconstriction to vasodilation.* Am J Physiol Heart Circ Physiol, 2003. **285**(1): p. H241-50.
170. Crider, A. and A. Pillai, *Estrogen Signaling as a Therapeutic Target in Neurodevelopmental Disorders.* J Pharmacol Exp Ther, 2017. **360**(1): p. 48-58.

7. Appendix

Supplemental Table 1. Summary of behavioral assays of both *16p11.2*$^{df/+}$ and *16p11.2*^{Vasc} mice.

Model	16p11.2$^{df/+}$ mice				16p11.2^{Vasc} mice			
Sex	Male		Female		Male		Female	
Age	P14	P50	P14	P50	P14	P50	P14	P50
Behavior								
Home cage activity		Increased		Increased (no significant differences)		Increased (no significant differences)		Increased
Motor coordination		Better performance (no significant differences)		No significant differences		Decreased performance		Better performance
Marble burying		No significant differences		No significant differences		Increased		Increased (p=0.07)
Novel object recognition		Decreased interest in novel object		No significant differences		No significant differences		No significant differences
Social Interaction		Decreased interaction with female[147]				No significant differences		No significant differences
Ultrasonic vocalization		Decrease number of calls[147]				No significant differences		No significant differences

Supplemental Table 2. Summary of functional assays of *16p11.2$^{df/+}$* and *16p11.2^{Vasc}* mice. Ach, acetylcholine; CBF, cerebral blood flow; L-NNA, NG-Nitro-L- arginine; PE, phenylephrine; SNP, sodium nitroprusside.

Model	16p11.2$^{df/+}$ mice				16p11.2^{Vasc} mice			
Sex	Male		Female		Male		Female	
Age	P14	P50	P14	P50	P14	P50	P14	P50
Function								
Baseline CBF	No significant differences	Increased	No significant differences	No significant differences		No significant differences		
% CBF increase	No significant differences	Decreased	No significant differences	No significant differences		Decreased		
Time to baseline	No significant differences	Increased	No significant differences	No significant differences		No significant differences		
Falling slope	No significant differences	Decreased	Decreased	No significant differences		Decreased		
Response amplitude	No significant differences	No significant differences	No significant differences	No significant differences		Decreased		
Time to max response	No significant differences	No significant differences	No significant differences	No significant differences		No significant differences		
Rising slope	No significant differences	Increased (p=0.07)	No significant differences	No significant differences		No significant differences		
Systolic blood pressure		No significant differences				No significant differences		
Heart rate		No significant differences				No significant differences		
Glucose uptake		Increased		Increased				
Oxygen saturation		No significant differences		No significant differences				
Middle cerebral artery response to acetylcholine		Impaired response (no dilation)		Impaired response (no dilation)				

Middle cerebral artery response to L-NNA		Impaired response (no constriction)		Impaired response (no constriction)				
Middle cerebral artery response to SNP		Normal response (dilation)		Normal response (dilation)				
Middle cerebral artery response to PE		Normal response (constriction)		Normal response (constriction)				
Middle cerebral artery response to adenosine		Impaired response (no dilation)		Impaired response (no dilation)				
Mesenteric artery response to acetylcholine		Impaired response (no dilation)						
Mesenteric artery response to PE		Normal response (dilation)						

Supplemental Table 3. Summary of structural differences of *16p11.2$^{df/+}$* and *16p11.2^{Vasc}* mice. VSMCs, vascular smooth muscle cells.

Model	16p11.2$^{df/+}$ mice				16p11.2^{Vasc} mice			
Sex	Male		Female		Male		Female	
Age	P14	P50	P14	P50	P14	P50	P14	P50
Structure								
Vascular density	Decreased	No significant differences (exception: increased in parietal cortex layer IV)	No significant differences	No significant differences	P0 Decreased (p=0.06)			
Vascular branching	Decreased	No significant differences (exception: increased in parietal cortex layer IV)	No significant differences	No significant differences	P0 Decreased			
Microglia Surface ratio Density	No significant differences	No significant differences						
Astrocyte Surface ratio Density	No significant differences (exception: increase in occipital cortex)	No significant differences						
VSMCs Surface ratio	No significant differences	No significant differences						
Pericyte Surface ratio Density	No significant differences	No significant differences						